Monthly Notices
of the
ROYAL ASTRONOMICAL SOCIETY

MNRAS **496,** 2613–2635 (2020)
Advance Access publication 2020 June 08

doi:10.1093/mnras/staa1594

LOFAR observations of X-ray cavity systems

L. Bîrzan,[1]★ D. A. Rafferty,[1] M. Brüggen,[1] A. Botteon,[2,3] G. Brunetti,[3] V. Cuciti,[1] A. C. Edge,[4] R. Morganti,[5,6] H. J. A. Röttgering[2] and T. W. Shimwell[5]

[1]*Hamburger Sternwarte, Universität Hamburg, Gojenbergsweg 112, D-21029 Hamburg, Germany*
[2]*Leiden Observatory, Leiden University, Oort Gebouw, PO Box 9513, NL-2300 RA Leiden, the Netherlands*
[3]*INAF – Instituto di Radioastronomia, via P. Gobetti, 101, I-40129 Bologna, Italy*
[4]*Institute for Computational Cosmology, Department of Physics, Durham University, Durham DH1 3LE, UK*
[5]*ASTRON, the Netherlands Institute for Radio Astronomy, Oude Hoogeveensedijk 4, NL-7991 PD Dwingeloo, the Netherlands*
[6]*Kapteyn Astronomical Institute, University of Groningen, PO Box 800, NL-9700 AV Groningen, the Netherlands*

Accepted 2020 June 2. Received 2020 May 30; in original form 2020 February 20

ABSTRACT

We present LOFAR observations at 120–168 MHz of 42 systems with possible X-ray cavities in their hot atmosphere, of which 17 are groups or ellipticals, 19 are nearby clusters ($z < 0.3$), and six are higher redshift clusters ($z > 0.3$). The X-ray cavities, formed by the radio lobes of the central active galactic nucleus (AGN), are evidence of radio-mode AGN feedback. In the groups and ellipticals sample, half of the systems have X-ray cavities for which no associated lobe emission was detected. Conversely, we report the discovery of large radio lobes in NGC 6338, extending far beyond the emission reported previously in the literature. In the case of the nearby clusters, our observations show that there is little low-frequency radio emission that extends beyond the cavities (e.g. MS 0735.6+7421, A2052). For the first time, we report secure cavity-radio associations in 2A 0335+096, ZwCl 2701, and ZwCl 8276 that strengthens their interpretation as AGN-created cavities. However, in some known cavity systems (e.g. A1795 and ZwCl 3146) we report the lack of detectable low-frequency radio emission associated with the cavities. Our sample of higher redshifts systems is small, and unfortunately the present LOFAR observations are not able to resolve the lobes in many of them. Nevertheless, our sample represents one of the best available for investigating the connection between radio and jet power in radio-mode AGN feedback.

Key words: X-rays: galaxies: clusters – radio continuum: galaxies.

1 INTRODUCTION

The AGN feedback paradigm in galaxy clusters posits that the central active galactic nucleus (AGN) is connected in a feedback loop to the cooling intracluster medium (ICM) in which the AGN resides (see the reviews, McNamara & Nulsen 2007; Fabian 2012). This feedback is generally negative, such that when the cooling increases the AGN heating increases to compensate, reducing the cooling. AGN feedback has been observed in systems ranging from massive clusters to isolated ellipticals (e.g. Cavagnolo et al. 2008; Rafferty, McNamara & Nulsen 2008; Voit et al. 2008; Hogan et al. 2015; Babyk et al. 2019; Lakhchaura et al. 2018; Pulido et al. 2018). Sophisticated AGN feedback simulations, when they account for both negative AGN feedback (e.g. Gaspari, Ruszkowski & Oh 2013; Li & Bryan 2014a; Prasad, Sharma & Babul 2015, 2017; Yang & Reynolds 2016; Gaspari & Sądowski 2017; Meece, Voit & O'Shea 2017; Martizzi et al. 2019; Wang et al. 2019) and positive AGN feedback (e.g. feedback that enhances the cooling and star formation (SF) activity; Gaibler et al. 2012; Wagner, Bicknell & Umemura 2012; Silk 2013; Wagner et al. 2016; Valentini et al. 2020), have demonstrated its importance to galaxy formation and evolution. For example, AGN feedback provides a mechanism to truncate cooling in massive galaxies (Croton et al. 2006; Alexander & Hickox 2012; Sijacki et al. 2015; Croton et al. 2016; Wylezalek & Zakamska 2016; Dekel, Lapiner & Dubois 2019), to reconcile the SF history of the largest elliptical galaxies with those predicted from hierarchical clustering through dry mergers (Faber et al. 2007), and to prevent overcooling of the ICM in the cooling-flow clusters (the cooling flow problem, Fabian 1994).

Direct observational evidence for AGN feedback comes from high-angular resolution *Chandra* X-ray observations of giant elliptical galaxies, groups, and clusters that contain large amounts of hot plasma. These observations show X-ray cavities in the hot atmospheres, filled with radio emission from the lobes of the central radio source associated with the brightest cluster galaxy (BCG). To date, *Chandra* has discovered ∼100 such systems (see cavity samples, Bîrzan et al. 2004, 2012; Dunn & Fabian 2004; Dunn, Fabian & Sanders 2006; Rafferty et al. 2006; Nulsen et al. 2009; Cavagnolo et al. 2010; Dong, Rasmussen & Mulchaey 2010; Dunn

★ E-mail: lbirzan@hs.uni-hamburg.de

et al. 2010; O'Sullivan et al. 2011; Hlavacek-Larrondo et al. 2012; Hlavacek-Larrondo et al. 2015; Shin, Woo & Mulchaey 2016; Bîrzan et al. 2017). The X-ray cavities are direct evidence of a strong coupling between the AGN jets and the hot atmospheres (see the reviews of McNamara & Nulsen 2007; Cattaneo et al. 2009; Fabian 2012; McNamara & Nulsen 2012; Voit et al. 2015). This feedback mode is known in the literature as the *maintenance-mode* or *radio-mode* feedback, to distinguish it from the radiatively dominated quasar-mode feedback.

In *radio-mode AGN feedback*, the heating is thought to be mainly done by the buoyantly rising cavities created by the AGN, along with the weak shocks (Nulsen et al. 2005; Randall et al. 2015; Forman et al. 2017), sound waves (Fabian et al. 2003; Fabian et al. 2017; Tang & Churazov 2017), subsonic turbulence through gravity waves, g modes (Reynolds, Balbus & Schekochihin 2015; Bambic, Morsony & Reynolds 2018), mixing of the inflated cavity's contents with the ICM (Brüggen & Kaiser 2002; Hillel & Soker 2017), shocks and turbulent mixing (Yang & Reynolds 2016), internal waves, and turbulence mixing (Kim & Narayan (Kim & Narayan 2003; Gaspari et al. 2014; Zhuravleva et al. 2014, 2018; Gaspari, Brighenti & Temi 2015; Zhang, Churazov & Schekochihin 2018), cosmic rays (CR; Guo & Oh 2008; Pfrommer 2013; Jacob & Pfrommer 2017; Ruszkowski, Yang & Reynolds 2017), and uplifting of the cool, central gas by the expanding jets and rising cavities (Peterson & Fabian (Peterson & Fabian 2006; Revaz, Combes & Salomé 2008; Pope et al. 2010; Li & Bryan 2014a; Brighenti, Mathews & Temi 2015; Kirkpatrick & McNamara 2015; McNamara et al. 2016; Gendron-Marsolais et al. 2017; Voit et al. 2017). It is not yet established which of these processes is the dominant source of heat, but there is a consensus that the heating is self-regulated in a gentle process, as the entropy increases continuously from the centre to the cluster outskirts (e.g. Voit et al. 2017). Furthermore, it is also important to connect all these processes responsible for AGN feedback and feeding from the smallest scales (micro scales) to the largest (meso and macro scales, Gaspari, Tombesi & Cappi 2020). However, proper modelling of the multiphase nature of the cooling gas that occurs on small scales is computationally challenging, and next generation simulations are likely needed to detangle this problem (Jiang & Oh 2018; Ogiya et al. 2018; Martizzi et al. 2019).

The X-ray cavities seen in groups and clusters are not only direct evidence of the interplay between the radio source and the ICM, they also allow one to systematically quantify the bulk of the energy injected by the AGN into the cluster atmosphere by measuring the work done by the buoyantly rising cavities (Bîrzan et al. 2004; Dunn et al. 2006; Rafferty et al. 2006; Bîrzan et al. 2012; Hlavacek-Larrondo et al. 2012). Until recently, cavities were detected at redshifts up to $z = 0.544$ (e.g. MACS J1423.9+2404, Rafferty et al. 2006; Hlavacek-Larrondo et al. 2012), but with the advent of the Sunyaev–Zel'dovich selected samples of clusters (e.g. SPT, ACT, Planck; Reichardt et al. 2013; Marriage et al. 2011; Planck Collaboration XXIX 2014), there are now cavity candidates up to $z = 1.132$ (e.g. SPT-CL J2106-5845; Bîrzan et al. 2017). However, at these high redshifts the details of the AGN feedback process are even less well understood, with some evidence that the primary mode of feedback transitions from a mechanically dominated mode to a radiatively dominated one, e.g. from low-excitation radio galaxies (LERGs) to high-excitation radio galaxies (HERGs),[1] or radio mode to quasar mode feedback (Churazov et al. 2005; Russell et al. 2013; Hlavacek-Larrondo et al. 2013b; Bîrzan et al. 2017; McDonald et al. 2018; Pinto et al. 2018).

An important result from X-ray cavity studies is the determination of scaling relations between the cavity power and the radio power (Bîrzan et al. 2004; Merloni & Heinz 2007; Bîrzan et al. 2008; Cavagnolo et al. 2010; O'Sullivan et al. 2011; Heckman & Best 2014). There is a large range of (logarithmic) slopes found in these scaling relations (e.g. from 0.35 to 0.75 in the case of monochromatic relations at 1.4 GHz; Bîrzan et al. 2008; Cavagnolo et al. 2010; O'Sullivan et al. 2011), with the latter relation spanning over seven orders of magnitude in radio and jet power. At 325 MHz, the best-fitting relation has a slope of ≈0.5 (Bîrzan et al. 2008; Kokotanekov et al. 2017). There is also a difference in the above scaling relation slopes if with some information on the spectral age of the lobe emission, through the break frequency of the synchrotron spectrum (e.g. for the scaling relations of the cavity power versus the bolometric radio luminosity a slope of 0.5 or 0.6 was found for the total source or lobes only versus 0.7 when the break frequency information is included; Bîrzan et al. 2008). With the break frequency included, the scatter about the best-fitting relation is reduced by ∼ 50 per cent (Bîrzan et al. 2008).

These scaling relations have been used for a variety of purposes by a number of authors, e.g. for studies of how jet-mode heating balances cooling for large samples of galaxies (e.g. Best et al. 2006, 2007; Magliocchetti & Brüggen 2007; Hart, Stocke & Hallman 2009; Ma, McNamara & Nulsen 2013; Best et al. 2014), for studies of the cosmic evolution of AGN feedback to higher redshifts (e.g. Cattaneo & Best 2009; Smolčić et al. 2009; Danielson et al. 2012; Simpson et al. 2013; Best et al. 2014; Smolcic et al. 2015; Pracy et al. 2016; Smolčić et al. 2017; Hardcastle et al. 2019), and for studies of the accretion mechanism and accretion rates (Sun 2009; Sabater et al. 2019). While fairly uncertain, for a sample with a wide range in luminosities a slope of ∼0.7 is widely used (see discussion in Best et al. 2006; Cattaneo et al. 2009; Heckman & Best 2014; Smolčić et al. 2017; Hardcastle et al. 2019).

Additionally, there are also theoretical models for the scalings derived from FanaroffRiley type II (FRII; Fanaroff & Riley 1974) expansion models (Willott et al. 1999; Daly et al. 2012; Ineson et al. 2017). From theoretical considerations, the slope is expected to range from 0.5 according to buoyancy arguments (Godfrey & Shabala 2016) to 0.8 according to FRII modelling (Willott et al. 1999; Daly et al. 2012). As a result, it is important to better constrain and understand the observed slopes and to understand whether they are in conflict with the theoretical ones. This point is especially true for FanaroffRiley type I (FRI) sources that constitute the majority of radio sources observed in cluster centres (see also the FRI source model, Luo & Sadler 2010). It is also important to understand whether there are variations in the slope that depend on environment and redshift; for example, for radio sources in groups/elliptical category, in order to explain the lower average kinetic power of the jets, deceleration of the jets by mass entrainment was invoked (Bicknell 1984; Laing & Bridle 2014; Perucho et al. 2014). This deceleration may have an effect on the spectral age of the source, which could in turn affect the slope of the radio to jet-power scaling. Our goal is to use LOFAR observations to better constrain the scaling relations at lower frequencies, adding information regarding the spectral shape, and to increase the sample at lower luminosities and higher redshifts.

In this paper, we present LOFAR observations at 120–168 MHz for 42 systems with likely cavities, ranging from ellipticals to massive clusters. Our goal is to supplement our previous sample (Bîrzan et al. 2008) with additional systems, and we particularly focus on groups and ellipticals and higher redshift clusters ($z >$

[1]LERG versus HERG dichotomy is based on the presence of weak, narrow low-ionization lines (Hine & Longair 1979; Hardcastle, Evans & Croston 2006, 2007).

0.3), which had very little representation in Bîrzan et al. (2008) sample. We also expand the lower redshift clusters sample ($z < 0.3$), since we want to ensure that we have a wide distribution of halo masses. We will present an analysis of the low-frequency jet power to radio power scaling relations in a subsequent paper. The paper is organized as follows: the sample is presented in Section 2, details of the X-ray (*Chandra*) and radio (LOFAR) data analysis are presented in Section 3, our results and discussion in Sections 4 and 5, respectively, and our conclusions in Section 6.

2 THE SAMPLE

Our sample consists of 42 systems with possible X-ray cavities observed with LOFAR (see Tables 1–3), based on the cavity sample of Bîrzan et al. (2008) (called the B08 sample henceforth) of systems with multifrequency Very Large Array (VLA) radio data at four frequencies (327 MHz, 1.4 GHz, 4.5 GHz, and 8.5 GHz) and at high-angular resolution (e.g. ≈1.0 arcsec × 1.0 arcsec at 1.4 GHz, A array). These systems are highlighted in bold in Tables 1–3. The B08 sample consists of 5 groups and ellipticals, two high-redshift clusters, and 17 nearby clusters. In the B08 sample we were able to separate the lobe versus core radio emission for a subsample of 12 systems (4 groups and 8 nearby clusters). For the remaining systems, the lobe break frequency could not be well constrained, either because the data did not sample the emission at low enough frequencies or because the lobes could only be detected and resolved at one frequency (e.g. A1835).

From the original B08 sample, we imaged the majority of the systems that could be observed with LOFAR (those situated at $\delta_{2000} > +0°$).[2] More recently, Kokotanekov et al. (2017) imaged many of these systems with LOFAR at 140 MHz, but at a resolution of only ≈23 arcsec × 23 arcsec. The main goal of this paper is to expand the low-frequency imaging of Kokotanekov et al. (2017) to higher resolutions and to systems at higher redshifts and with lower X-ray luminosities (i.e. groups and ellipticals).

In order to expand the B08 sample to lower luminosity systems, we identified known groups and ellipticals with X-ray cavities in the literature (e.g. Rafferty et al. 2006; Cavagnolo et al. 2010; Dong et al. 2010; Dunn et al. 2010; O'Sullivan et al. 2011) that are accessible to LOFAR. To this end, we limited our sample to systems that lie at $\delta_{2000} > +0°$, but in principle even lower declinations are accessible, although LOFAR's sensitivity declines as the projected area of the stations decreases. Also, we added a number of ellipticals which likely harbour cavities and where significant H α emission is present (e.g. NGC 499, NGC 410; Lakhchaura et al. 2018).

Additionally, we also expanded the lower redshift ($z < 0.3$) cluster sample. This was done by adding a number of clusters found recently to have cavities that are not present in the B08 sample, e.g. 4C+55.16 (Rafferty et al. 2006), ZwCl 8276 (Ettori et al. 2013), A2390 (Savini et al. 2019), RX J0820.9+0752 (Vantyghem et al. 2019), A1361, ZwCl 0235, RX J0352.9+1941, MS 0839.9+2938 (Shin et al. 2016). We also included some cooling flow clusters that might harbor cavities and where significant H α emission is present (e.g. A1668, ZwCl 0808; Crawford et al. 1999). To expand the sample to higher redshifts ($z > 0.3$), we used the sample of Hlavacek-Larrondo et al. (2012) supplemented with some putative cavity systems from Shin et al. (2016), e.g. MACS J1621.3+3810.

In the Table (1– 3), systems are grouped into three categories: groups and ellipticals, nearby clusters ($z < 0.3$), and higher redshift clusters ($z > 0.3$), all of them ordered from lower to higher redshift. However, it is important to mention that there is an overlap between these categories, due to the range of mass, radio power, and redshift. Furthermore, at the end of each category, we list the systems for which LOFAR observations from this paper failed to find radio emission filing the reported X-ray cavities (e.g. A1795, MACS J1359.8+6231, NGC 3608, and NGC 777). Throughout this paper we use the term *radio-filled cavities*; the radio association is interpreted as clear evidence for radio-mode AGN feedback (see the summary table, Table 3).

Lastly, in Table 3, we also added available information from the literature regarding the presence of H α filaments or molecular gas and evidence for sloshing. The H α filaments and the molecular gas imaged in nearby groups and clusters are interpreted as the end product of the cooling of the X-ray gas (e.g. the chaotic cold accretion mechanism; Gaspari et al. 2013), and they have a diverse range of morphologies (e.g. discs, filaments, etc. Hamer et al. 2016). Sloshing, in which the BCG oscillates around the cluster centre, is thought to be due to a perturbation of the gravitational potential of the cluster that follows an off-axis minor merger (Markevitch et al. 2000; Markevitch & Vikhlinin 2007). It has been postulated that such sloshing might produce enough heating to balance the cooling of the inner regions ($r \lesssim 30$ kpc; ZuHone, Markevitch & Johnson 2010). Information on the presence of sloshing, H α filaments, and molecular gas can be used to understand whether heating by sloshing and the presence of molecular gas and H α filaments are common in systems with X-ray cavities.

3 DATA ANALYSIS

3.1 LOFAR data

All systems were observed with the high-band array (HBA) of LOFAR at frequencies of 120–168 MHz (for observational details see Table 2). Most systems were observed as part of LoTSS, the LOFAR Two-meter Sky Survey (Shimwell et al. 2019), and for 8 h of total integration time, except for the lower declination systems that were observed for 4 h (see Table 2).[3] The PREFACTOR[4] and FACTOR pipelines[5] were used to calibrate and image the data using the facet-calibration scheme described in van Weeren et al. (2016), following the process detailed in Bîrzan et al. (2019). Version 2.0.2 of PREFACTOR and version 1.3 of FACTOR were used. A conservative systematic uncertainty of 15 per cent was adopted on all LOFAR flux densities throughout our analysis, as done in previous LOFAR-HBA work (see Table 2 for the total flux density, the rms noise, and the resolution of the final image).

3.2 X-ray data

Table 1 lists information on the *Chandra* X-ray observations used in this work, such as the observation IDs, the total integration time on

[2]From the B08 sample, two groups (Centaurus and HCG 62) and five nearby clusters (A133, Hydra A, Sersic 159/03, A2597, and A4059) lie at $\delta_{2000} < +0°$. The B08 systems missing from our sample that are situated at $\delta_{2000} > +0°$ are Perseus, M84, and M87, for which the LOFAR reduction is non-trivial due to the presence of very bright sources, RBS 797, MACS J0423.8+2402, and A1835 (all works in progress), and Cygnus A, the LOFAR observations of which were already published by McKean et al. (2016).

[3]In the case of not target on source observations, such as the pointings of the LoTSS, there will be a lower effective integration time because of the primary beam attenuation (≈4–8 h effective integration time).

[4]Available at https://github.com/lofar-astron/prefactor

[5]Available at https://github.com/lofar-astron/factor

Table 1. *Chandra* observations.

System[a]	z	X-ray core (J2000) RA	Dec.	Obs. ID(ks)	Int.[b]	Cavities (Ref.)
Groups and ellipticals sample						
NGC 5846	0.005 71	15 06 29.25	+01 36 21.26	788, 7923	89.0	(8,13,23,29)
NGC 5813	0.006 53	15 01 11.27	+01 42 07.06	5907, 9517, 12951, 12952, 12953, 13246, 13247, 13253, 13255	588	(8,29,37)
NGC 193∗	0.014 72	00 39 18.57	+03 19 52.03	4053, 11389	95.8	(7,8,29)
A262∗	0.016	01 52 46.20	+36 09 11.80	2215, 7921	138.4	(5,9)
NGC 6338∗	0.027	17 15 22.90	+57 24 38.70	4194, 18892, 18893, 19934, 19935, 19937, 20089, 20104, 20112, 20113, 20117	295	(8,31,33,48)
IC1262∗	0.032 65	17 33 03.44	+43 45 34.59	2018, 6949, 7321, 7322	134.7	(10,34)
NGC 6269∗	0.034 80	16 57 58.08	+27 51 15.85	4972	37.3	(1,8,29)
NGC 5098∗	0.037 89	13 20 14.73	+33 08 36.05	6941	36.5	(10,36)
.....						
NGC 741	0.018 55	01 56 20.97	+05 37 44.26	2223, 17198, 18718	170	(10,19,20,40)
NGC 3608	0.004 09	11 16 59.34	+18 08 51.90	2073	32.8	(8)
NGC 2300	0.006 35	07 32 18.86	+85 42 32.26	4968, 15648	51.1	(10)
NGC 499∗	0.014 67	01 23 11.51	+33 27 36.33	10523, 10865, 10866, 10867	38.5	...
NGC 777	0.016 73	02 00 14.90	+31 25 44.95	5001	9.0	(8)
NGC 410	0.017 66	01 10 58.92	+33 09 06.76	5897	2.6	...
UGC 5088	0.026 93	09 33 25.69	+34 02 53.46	3227	28.4	(10)
NGC 4104∗	0.0282	12 06 38.88	+28 10 24.76	6339	36.0	(41)
RX J1159.8+5531	0.081	11 59 52.23	+55 32 06.68	4964	64.8	(10)
Nearby clusters sample ($z<0.3$)						
A2199	0.030	16 28 38.20	+39 33 04.94	10748, 10803, 10804, 10805	118.8	(2,11,21,28,32)
2A0335+096	0.035	03 38 40.90	+09 58 04.62	919, 7939, 9792	100	(2,25,38)
A2052	0.035	15 16 44.46	+07 01 17.88	5807, 10477, 10478, 10479, 10480 10879, 10914, 10915, 10916,10917	612	(2,3,4,6,11)
MKW3S	0.045	15 21 51.80	+07 42 31.0	900		(2,11,24)
A1668	0.0643	13 03 46.60	+19 16 12.20	12877	9.7	...
ZwCl 8276∗	0.0757	17 44 14.45	+32 59 29.31	8267, 11708	52.1	(14)
A478	0.081	04 13 25.35	+10 27 54.70	1669, 6102	52.4	(2,12,43)
A1361	0.117	11 43 39.76	+46 21 21.21	3369	1.0	(41,49)
ZwCl 0808∗	0.169	03 01 38.19	+01 55 14.98	12253	16.6	...
ZwCl 2701∗	0.214	09 52 49.25	+51 53 05.32	3195, 12903	117.5	(35,44)
MS 0735.6+7421	0.216	07 41 44.66	+74 14 36.85	4197, 10468, 10469, 10470, 10471, 10822, 10918, 10922	465.7	(15,26,27,45)
A2390	0.234	21 53 36.85	+17 41 42.35	500, 4193	89.5	(39,41,42)
4C+55.16	0.241	08 34 54.90	+55 34 20.90	1645, 4940	75.8	(16,35)
.....						
A1795	0.063	13 48 52.30	+26 35 36.78	493, 3666, 5286, 5287, 5288, 5289, 5290, 6160, 6163, 10900, 12026, 12027, 13108, 13109, 13110, 13111, 13113, 14270, 14271	292	(2,12,22,47)
ZwCl 0235∗	0.083	00 43 52.20	+24 24 22.0	11735	19.6	(41)
RX J0352.9+1941	0.109	03 52 59.02	+19 40 59.44	10466	27.2	(41)
RX J0820.9+0752	0.110 87	08 21 02.30	+07 51 46.39	17194, 17563	64.4	(46)
MS 0839.9+2938∗	0.194	08 42 55.90	+29 27 26.90	2224	26.7	(41)
ZwCl 3146∗	0.291	10 23 39.57	+04 11 12.92	909, 9371	74.1	(35)
High-redshift clusters sample ($z>0.3$)						
MACS J1532.9+3021	0.363	15 32 53.74	+30 20 58.50	1649, 1665, 14009	104.6	(17,18)
IRAS 09104+4109∗	0.442	09 13 45.49	+40 56 27.92	10445	68.9	(17,30)
MACS J1621.3+3810	0.465	16 21 24.75	+38 10 07.58	3254, 6109, 6172, 9379, 10785	123	(41,49)
.....						
MACS J2245.0+2637	0.301	22 45 04.54	+26 38 04.45	3287	11.8	(17)
MACS J1359.8+6231∗	0.330	13 59 50.51	+62 31 05.58	516, 7714	29.3	(17)
MACS J1720.2+3536	0.3913	17 20 16.90	+35 36 28.85	3280, 6107, 7718	53.1	(17)

Notes. References: (1) Baldi et al. (2009); (2) Bîrzan et al. (2004); (3) Blanton et al. (2001); (4) Blanton, Sarazin & McNamara (2003); (5) Blanton et al. (2004); (6) Blanton et al. (2011); (7) Bogdán et al. (2014); (8) Cavagnolo et al. (2010); (9) Clarke et al. (2009); (10) Dong et al. (2010); (11) Dunn & Fabian (2004); (12) Dunn, Fabian & Taylor (2005); (13) Dunn et al. (2010); (14) Ettori et al. (2013); (15) Gitti et al. (2007); (16) Hlavacek-Larrondo et al. (2011); (17) Hlavacek-Larrondo et al. (2012); (18) Hlavacek-Larrondo et al. (2013a); (19) Jetha et al. (2007); (20) Jetha et al. (2008); (21) Johnstone et al. (2002); (22) Kokotanekov et al. (2018); (23) Machacek et al. (2011); (24) Mazzotta et al. (2002); (25) Mazzotta et al. (2003); (26) McNamara et al. (2005); (27) McNamara et al. (2009); (28) Nulsen et al. (2013); (29) O'Sullivan et al. (2011); (30) O'Sullivan et al. (2012); (31) O'Sullivan et al. (2019); (32) Owen & Eilek (1998); (33) Pandge et al. (2012); (34) Pandge et al. (2019); (35) Rafferty et al. (2006); (36) Randall et al. (2009); (37) Randall et al. (2015); (38) Sanders, Fabian & Taylor (2009); (39) Savini et al. (2019); (40) Schellenberger et al. (2017); (41) Shin et al. (2016); (42) (Sonkamble et al. 2015); (43) Sun et al. (2003); (44) Vagshette et al. (2016); (45) Vantyghem et al. (2014); (46) Vantyghem et al. (2019); (47) Walker et al. (2014); (48) Wang et al. (2019); (49) this work.

[a]The systems in bold are from B08 sample. The asterisk marks systems with alternative names, as in Table 2.

[b]Total integration time on source, after reprocessing.

Table 2. 143 MHz LOFAR observations.

System[a]	z	Obs. date[b]	Total flux density (Jy)	Rms noise (μJy beam^{-1})	Resolution (arcsec × arcsec)	Radio (Ref.)
Groups and ellipticals sample						
NGC 5846	0.00571	01-09-2018∗	0.091 ± 0.017	780	14.07 × 5.93	(10,21)
NGC 5813	0.00653	01-09-2018∗	0.066 ± 0.013	430	14.06 × 5.9	(10)
NGC 193∗	0.01472	06-06-2019∗	6.16 ± 0.93	360	13.42 × 5.76	(10,20)
A262∗	0.016	23-05-2014	0.576 ± 0.090	585	14.41 × 10.76	(2,5,7,16,29)
NGC 6338∗	0.027	21-12-2017	0.160 ± 0.025	138	13.66 × 8.68	(16,25,38)
IC 1262∗	0.03265	13-06-2018	5.61 ± 0.85	180	7.86 × 4.52	(16,28,32)
NGC 6269∗	0.03480	25-01-2017	0.272 ± 0.042	250	8.48 × 6.21	(1,9,10,16)
NGC 5098∗	0.03789	10-05-2018	0.186 ± 0.033	733	7.87 × 5.17	(16,31)
.....						
NGC 741	0.01855	09-06-2019∗	3.90 ± 0.60	513	13.33 × 5.73	(10,17,36)
NGC 3608	0.00409	11-01-2018	...	636	9.32 × 5.49	...
NGC 2300	0.00635	26-07-2017	0.006 ± 0.002	198	8.16 × 5.09	...
NGC 499∗	0.01467	28-10-2016	0.046 ± 0.009	585	8.75 × 5.76	...
NGC 777	0.01673	24-10-2016	0.032 ± 0.006	246	8.42 × 5.13	...
NGC 410	0.01766	08-08-2016	0.039 ± 0.007	520	11.05 × 4.91	...
UGC 5088	0.02693	01-09-2018	0.003 ± 0.001	140	5.59 × 3.27	...
NGC 4104∗	0.0282	04-04.2017	0.018 ± 0.004	184	9.09 × 5.84	(16)
RX J1159.8+5531	0.081	15-02-2015	0.004 ± 0.001	83	8.6 × 5.18	...
Nearby clusters sample ($z<0.3$)						
A2199	0.030	24-03-2016	53.97 ± 8.10	850	7.47 × 4.69	(2,4,13,27)
2A0335+096	0.035	04-01-2018	0.852 ± 0.135	1100	9.79 × 5.91	(2,30,33,34)
A2052	0.035	14-08-2014	58.53 ± 8.82	4925	8.80 × 6.51	(2,3,40)
MKW3S	0.045	14-08-2014	21.24 ± 3.20	726	8.80 × 6.51	(2,9,23)
A1668	0.0643	05-04-2019	1.83 ± 0.44	286	10.21 × 6.52	(16)
ZwCl 8276∗	0.0757	30-05-2018	0.90 ± 0.14	468	8.29 × 5.20	(11,16)
A478	0.081	...	...	...	...	(2,11,16,35)
A1361	0.117	15-06-2014	5.22 ± 0.8	1030	12.46 × 5.41	(16,26)
ZwCl 0808∗	0.169	17-07-2018∗	11.64 ± 1.78	4070	13.0 × 5.75	(16)
ZwCl 2701∗	0.214	20-02-2018	1.34 ± 0.20	204	7.75 × 4.43	(2,37)
MS 0735.6+7421	0.216	18-05-2013	4.33 ± 0.65	404	9.65 × 8.23	(1,22)
A2390	0.234	...	...	...	...	(16,35)
4C+55.16	0.241	15-06-2019	11.74 ± 1.77	1350	8.92 × 2.91	(6,39)
.....						
A1795	0.063	03-05-2014	6.45 ± 0.98	1610	10.14 × 5.93	(2,8,11)
ZwCl 0235∗	0.083	28-09-2018	0.151 ± 0.024	387	9.34 × 6.15	(16)
RX J0352.9+1941	0.109	03-07-2018	0.068 ± 0.011	157	8.91 × 5.53	(16)
RX J0820.9+0752	0.11087	08-29-2018	0.021 ± 0.004	590	13.29 × 5.38	(16)
MS 0839.9+2938	0.194	18-02-2016	0.221 ± 0.035	331	10.51 × 5.40	(12)
ZwCl 3146∗	0.291	08-06-2018∗	0.055 ± 0.009	765	14.20 × 5.23	(2,11,19)
High-redshift clusters sample ($z>0.3$)						
MACS J1532.9+3021	0.363	17-08-2018	0.097 ± 0.017	496	11.59 × 5.53	(6,11,15,16,18)
IRAS 09104+4109∗	0.442	01-02-2018	0.205 ± 0.033	582	8.76 × 5.35	(6,14,24)
MACS J1621.3+3810	0.465	20-08-2015	0.082 ± 0.015	707	8.68 × 5.47	(6)
.....						
MACS J2245.0+2637	0.301	14-07-2016	0.026 ± 0.006	594	9.15 × 6.19	...
MACS J1359.8+6231∗	0.330	29-09-2018	0.003 ± 0.002	310	8.23 × 5.6	...
MACS J1720.2+3536	0.3913	04-08-2018	0.172 ± 0.030	1004	7.54 × 4.9	...

Notes. References: (1) Baldi et al. (2009); (2) Bîrzan et al. (2008); (3) Blanton et al. (2011); (4) Burns, Schwendeman & White (1983); (5) Clarke et al. (2009); (6) Edge et al. (2003); (7) Fanti et al. (1987); (8) Ge & Owen (1993); (9) Giacintucci et al. (2007); (10) Giacintucci et al. (2011); (11) Giacintucci et al. (2014); (12) Giacintucci et al. (2017); (13) Giovannini et al. (1998); (14) Hines & Wills (1993); (15) Hlavacek-Larrondo et al. (2013a); (16) Hogan et al. (2015); (17) Jetha et al. (2008); (18) Kale et al. (2013); (19) Kale et al. (2015); (20) Laing et al. (2011); (21) Machacek et al. (2011); (22) McNamara et al. (2005); (23) Mazzotta et al. (2002); (24) O'Sullivan et al. (2012); (25) O'Sullivan et al. (2019); (26) Owen & Ledlow (1997); (27) Owen & Eilek (1998); (28) Pandge et al. (2019); (29) Parma et al. (1986); (30) Patnaik & Singh (1988); (31) Randall et al. (2009); (32) Rudnick & Lemmerman (2009); (33) Sanders et al. (2009); (34) Sarazin, Baum & O'Dea (1995); (35) Savini et al. (2019); (36) Schellenberger et al. (2017); (37) Vagshette et al. (2016); (38) Wang et al. (2019); (39) Xu et al. (1995); and (40) Zhao et al. (1993).

[a]For A478 and A2390, see Savini et al. (2019) for details of the LOFAR observations. The asterisk marks systems with alternative names: ZwCl 8276 (ZwCl 1742.1+3306); ZwCl 0808 (ZwCl 0258.9+0142); ZwCl 2701 (ZwCl 0949.6+5207); ZwCl 0235 (ZwCl 0040.8+2404); ZwCl 3146 (ZwCl 1021.0+0426); IRAS 09104+4109 (RX J0913.7+4056); MACS J1359.8+6231 (ZwCl 1358.1+6245, MS 1358.4+6245); NGC 193 (UGC408); A262 (NGC 708); NGC 6338 (RX J1715.3+5725); IC 1262 (RX J1733.0+4345); NGC 5098 (RXC J1320.2+3308); NGC 6269 (AWM 5, RX J1657.8+2751); NGC 499 (RX J0123.2+3327); NGC 4104 (RX J1206.6+2810).

[b]The integration time is 8 h, except for those with an asterisk for which it is 4 h.

source after reprocessing and the presence of cavities as reported in the literature. The X-ray data were reprocessed with CIAO 4.9[6] using CALDB 4.7.3[7] and used to make exposure-corrected X-ray images and residual maps, following the steps detailed in Rafferty et al.

[6]See cxc.harvard.edu/ciao/index.html.

[7]See cxc.harvard.edu/caldb/index.html.

Table 3. Summary.

System	z	Sloshing/ Cold fronts (Ref.)[a]	Hα filam./ Mol. gas[b] (Ref.)	Central-radio source with lobes[c] (yes/no)	Radio-filled cavities[d] (yes/no)
Groups and ellipticals sample					
NGC 5846	0.005 71	(17,21)	(19,21,35,40)	Yes	Yes
NGC 5813	0.006 53	...	(19,40)	Yes	Yes
NGC 193∗	0.014 72	...	(1)	Yes	Yes
A262∗	0.016	(18)	(4,9,34)	Yes∗	Yes
NGC 6338∗	0.027	(39)	(31)	Yes∗	Yes
IC 1262∗	0.032 65	(32)	(4)	Yes	Yes
NGC 6269∗	0.034 80	...	No (4)	Yes	?
NGC 5098∗	0.037 89	(33)	(4)	Yes	Yes
.....					
NGC 741	0.018 55	...	No (20)	Yes	No
NGC 3608	0.004 09	...	No (42)	No	No
NGC 2300	0.006 35	...	No (20)	No	No
NGC 499∗	0.014 67	...	(20)	No	No
NGC 777	0.016 73	...	No (20)	No	No
NGC 410	0.017 66	...	(20)	No	No
UGC 5088	0.026 93	...	...	No	No
NGC 4104∗	0.0282	...	(4)	No	No
RX J1159.8+5531	0.081	...	...	No	No
Nearby clusters sample ($z<0.3$)					
A2199	0.030	(18,28)	(27)	Yes	Yes
2A0335+096	0.035	(18,22)	(7,37)	Yes∗	Yes
A2052	0.035	(3)	(19,24)	Yes	Yes
MKW3S	0.045	...	(34,41)	Yes	Yes
A1668	0.0643	...	(19)	Yes∗	?
ZwCl 8276∗	0.0757	(12)	(4,9)	Yes∗	Yes
A478	0.081	...	(19,24)	Yes	Yes
A1361	0.117	...	(4)	Yes∗	Yes
ZwCl 0808∗	0.169	...	(4)	Yes∗	?
ZwCl 2701∗	0.214	...	(4)	Yes∗	Yes
MS 0735.6+7421	0.216	...	(26)	Yes	Yes
A2390	0.234	...	(19)	Yes∗	Yes
4C+55.16	0.241	...	(9)	Yes	Yes
.....					
A1795	0.063	(11,18)	(5,23,24,25,27,36)	Yes∗	No
ZwCl 0235∗	0.083	...	(4,34)	Yes∗	No
RX J0352.9+1941	0.109	...	(19)N	No	No
RX J0820.9+0752	0.110 87	...	(2,19,34,38)	No	No
MS 0839.9+2938	0.194	...	(6)	Yes	No
ZwCl 3146∗	0.291	(14,15)	(27,29)	Yes∗	No
High-redshift cluster sample ($z>0.3$)					
MACS J1532.9+3021	0.363	(16)	(8,13)	Yes	Yes
IRAS 09104+4109∗	0.442	(30)	(30)	Yes	Yes
MACS J1621.3+3810	0.465	...	(10)	Yes∗	Yes
.....					
MACS J2245.0+2637	0.301	...	...	?∗	No
MACS J1359.8+6231∗	0.330	...	(6)	No	No
MACS J1720.2+3536	0.3913	...	(8,13)	No	No

Notes. References: (1) Babyk et al. (2019); (2) Bayer-Kim et al. (2002); (3) Blanton et al. (2011); (4) Crawford et al. (1999); (5) Crawford et al. (2005); (6) Donahue, Stocke & Gioia (1992); (7) Donahue et al. (2007); (8) Donahue et al. (2015); (9) Edge et al. (2002); (10) Edge et al. (2003); (11) Ehlert et al. (2015); (12) Ettori et al. (2013); (13) Fogarty et al. (2015); (14) Forman et al. (2002a); (15) Forman et al. (2002b); (16) Hlavacek-Larrondo et al. (2013a); (17) Gastaldello et al. (2013); (18) Ghizzardi et al. (2010); (19) Hamer et al. (2016); (20) Lakhchaura et al. (2018); (21) Machacek et al. (2011); (22) Mazzotta et al. (2003); (23) McDonald & Veilleux (2009); (24) McDonald et al. (2010); (25) McDonald et al. (2014); (26) McNamara et al. (2009); (27) Mittal et al. (2015); (28) Nulsen et al. (2013); (29) O'Dea et al. (2010); (30) O'Sullivan et al. (2012); (31) Pandge et al. (2012); (32) Pandge et al. (2019); (33) Randall et al. (2009); (34) Salomé & Combes (2003); (35) Temi et al. (2018); (36) Tremblay et al. (2015); (37) Vantyghem et al. (2016); (38) Vantyghem et al. (2019); (39) Wang et al. (2019); (40) Werner et al. (2014); (41) White, Jones & Forman (1997); (42) Young et al. (2011).

[a]Indicates the presence of sloshing and/or cold fronts using information available in the literature.

[b]Indicates the presence of Hα filaments, and/or molecular gas using information available in the literature.

[c]Indicates the presence of a central radio source with resolved lobes (marked with 'yes'), and point source only emission or unresolved sources (marked with 'no'), and '?' for the sources with possible hints of resolved extended emission (radio lobes). The asterisk marks the systems for which the LOFAR data are a significant improvement over the previous observations and strengthen the evidence for AGN feedback in those systems.

[d]Systems for which the X-ray cavities are filled with lobe radio emission are marked with 'yes' and those without such emission with 'no'. The uncertain systems are marked with '?'.

(2013). To make the residual maps, a model of the extended X-ray emission is subtracted from the corresponding exposure-corrected image. The model was found using the multi-Gaussian expansion technique of Cappellari et al. (2006).

The X-ray and radio images for the systems in our sample are shown in Fig. 1 through Fig. 6 in three panels (*left-hand panels*: LOFAR images; *middle panels*: overlays of LOFAR contours and the X-ray residual maps; *right-hand panels*: smoothed X-ray

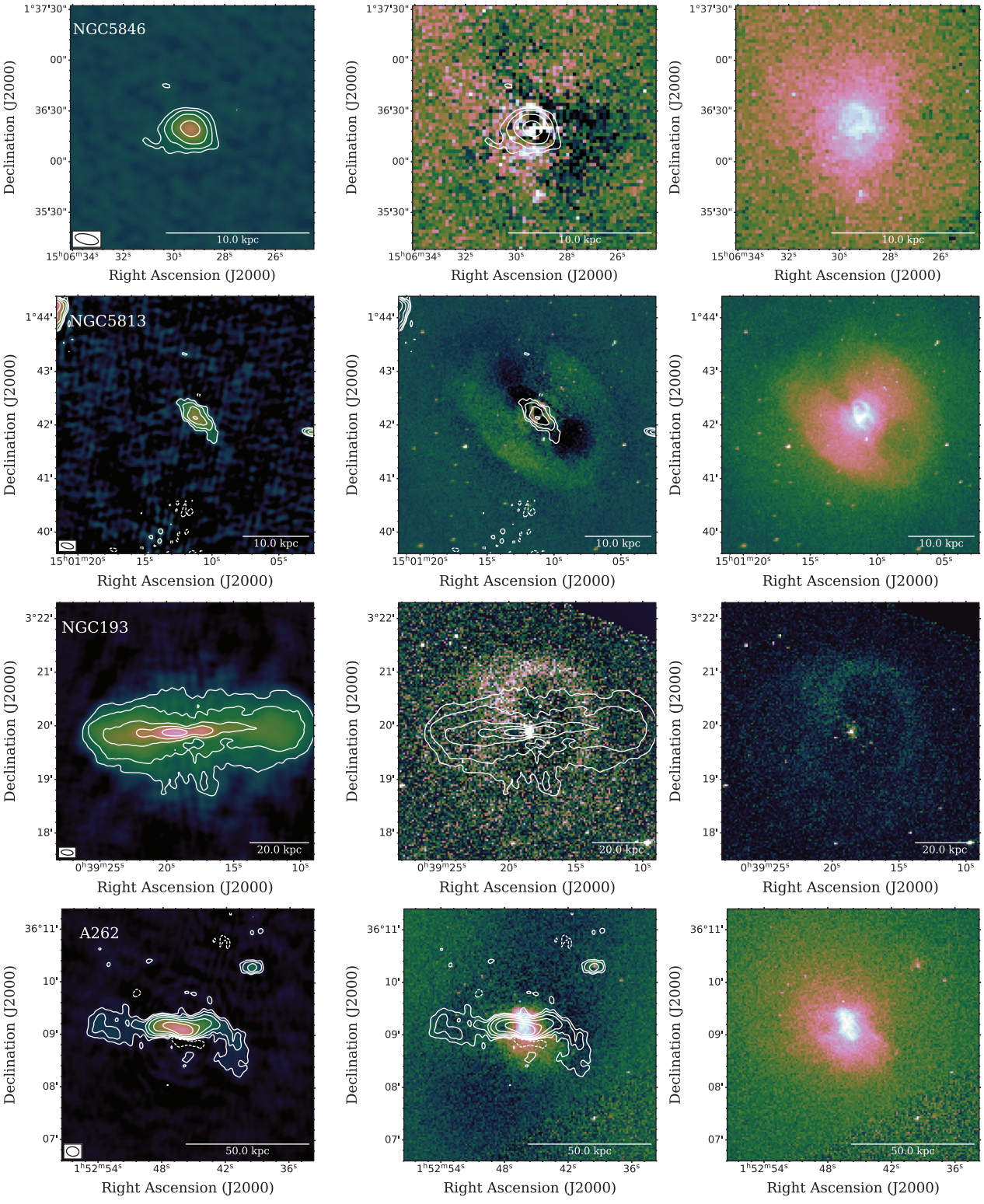

Figure 1. *Chandra* and LOFAR images for the groups and ellipticals with evident X-ray cavities, in the same order as in the tables (NGC 5846, NGC 5813, NGC 193, and A262 are shown above, NGC 6338, IC1262, NGC 6269, and NGC 5098 are shown in figure continued). *Left-hand panels*: LOFAR images at 143 MHz, the first contour is at 0.0026 (NGC 5846), 0.0018 (NGC 5813), 0.009 (NGC 193), 0.003 (A262), 0.00105 (NGC 6338), 0.00105 (IC1262), 0.0017 (NGC 6269), 0.018 mJy beam $^{-1}$ (NGC 5098) and each contour increases by a factor of two (the beam size is shown in the lower left-hand corner); *middle panels*: overlays of LOFAR contours and the X-ray residual maps; *right-hand panels*: smoothed X-ray images.

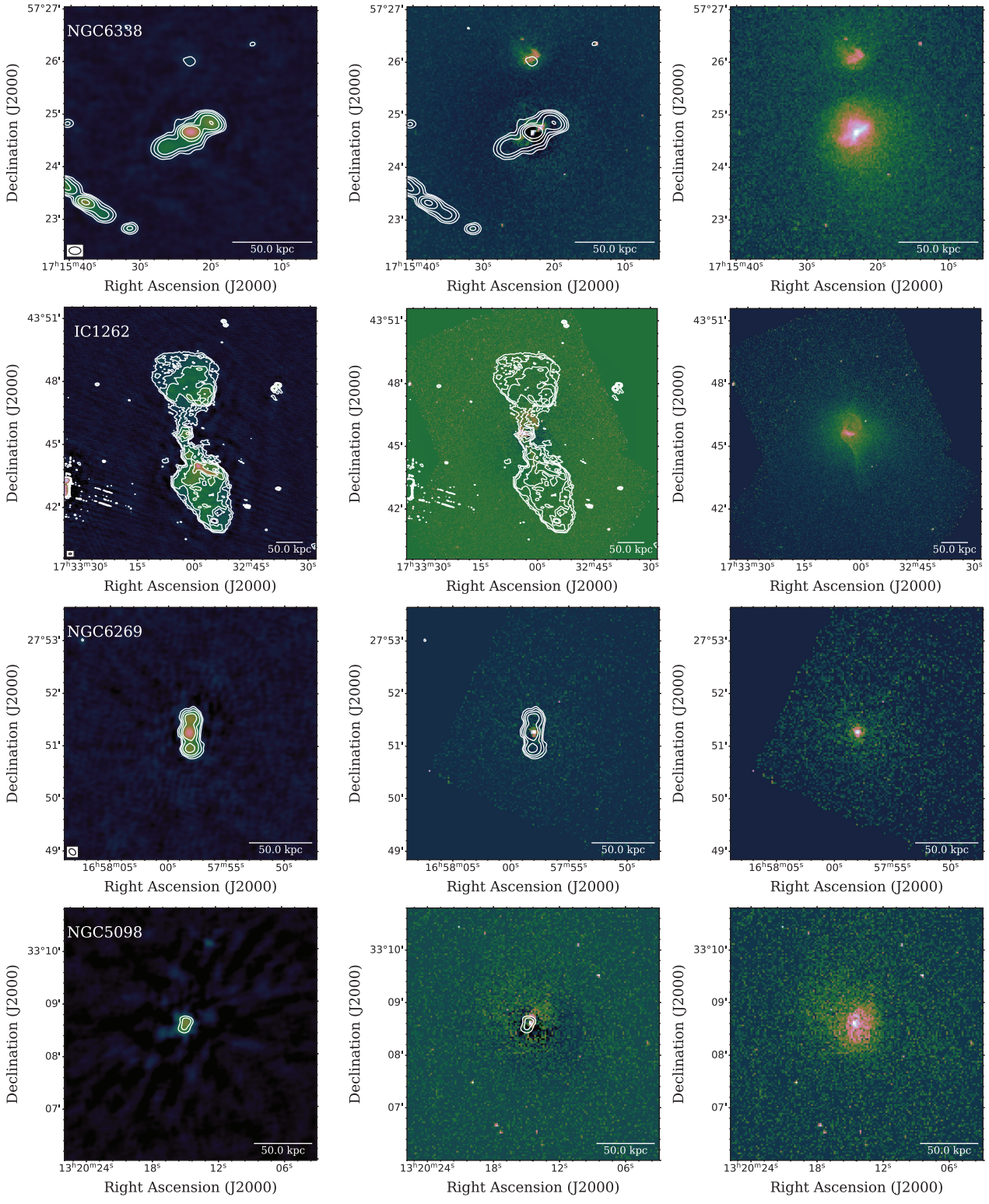

Figure 1. Continued.

images). The systems in the Figs (1–6) are shown in the same order as in the tables, starting with the groups and ellipticals with clear cavities (Fig. 1), groups and ellipticals without clear cavities (Fig. 2), nearby clusters with clear cavities (Fig. 3), nearby clusters without clear cavities (Fig. 4), high-redshift clusters with clear cavities (Fig. 5), and high-redshift clusters without clear cavities (Fig. 6).

4 RESULTS AND COMPARISON WITH PREVIOUS OBSERVATIONS

4.1 LOFAR images for B08 sample

The systems from the B08 sample are highlighted in bold in Tables 1–3 (see Section 2 for a summary of the B08 sample).

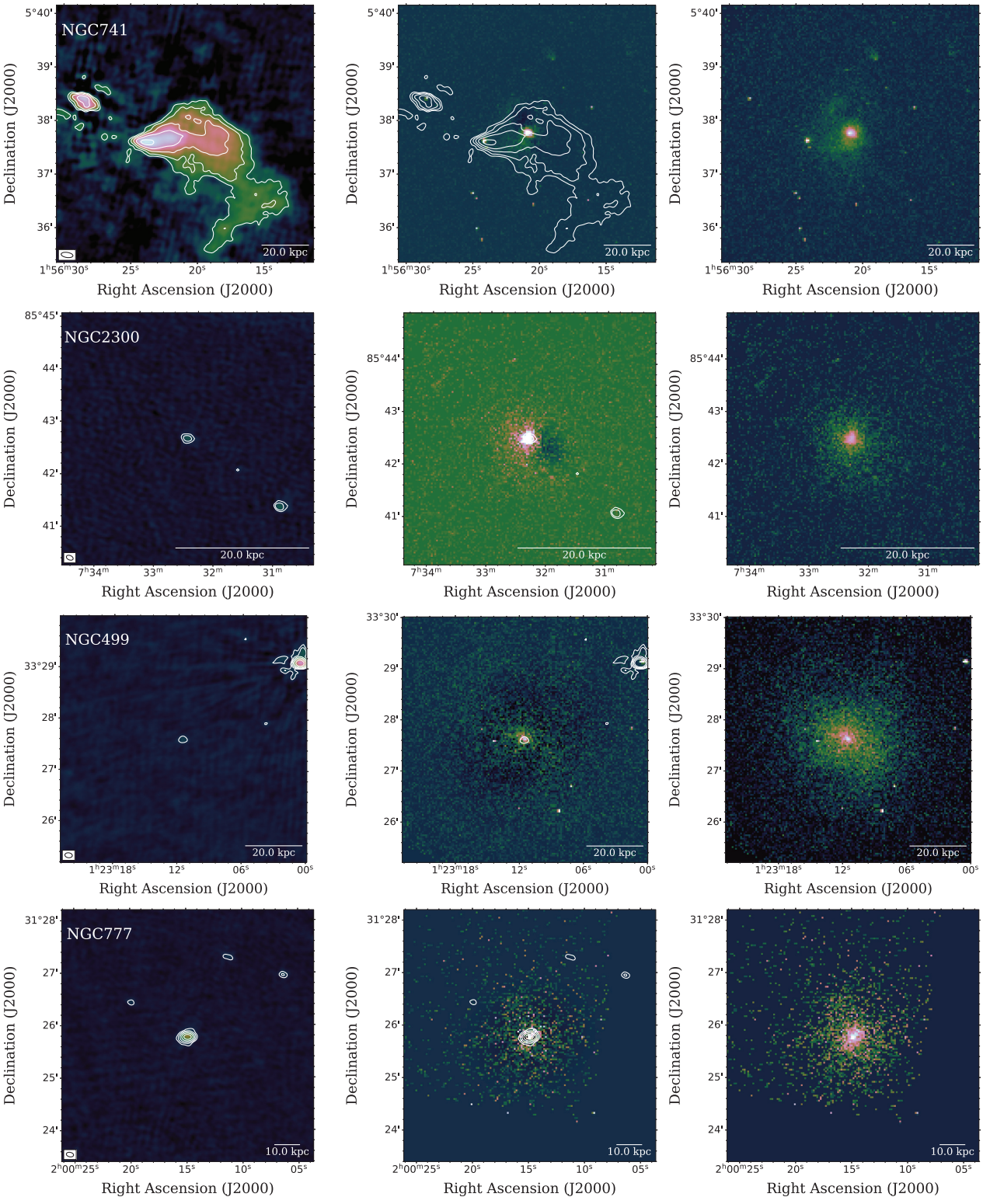

Figure 2. *Chandra* and LOFAR images for the groups and ellipticals with putative X-ray cavities which are not filled by radio emission, in the same order as in the tables (NGC 741, NGC 2300, NGC 499, and NGC 777 are shown above, NGC 410, UGC 5088, NGC 4104, and RX J1159.8+5531 are shown in figure continued). However, NGC 3608 is not shown since no central radio source was detected in the LOFAR image. The panel organization is the same as in Fig. 1. For the LOFAR image, the first contour is at 0.006 (NGC 741), 0.00096 (NGC 2300), 0.0021 (NGC 499), 0.00087 mJy beam^{-1}, (NGC 777) 0.0021 (NGC 410), 0.0012 (UGC 5088), 0.0012 (NGC 4104), 0.0006 mJy beam^{-1} (RX J1159.8+5531), and each contour increases by a factor of two.

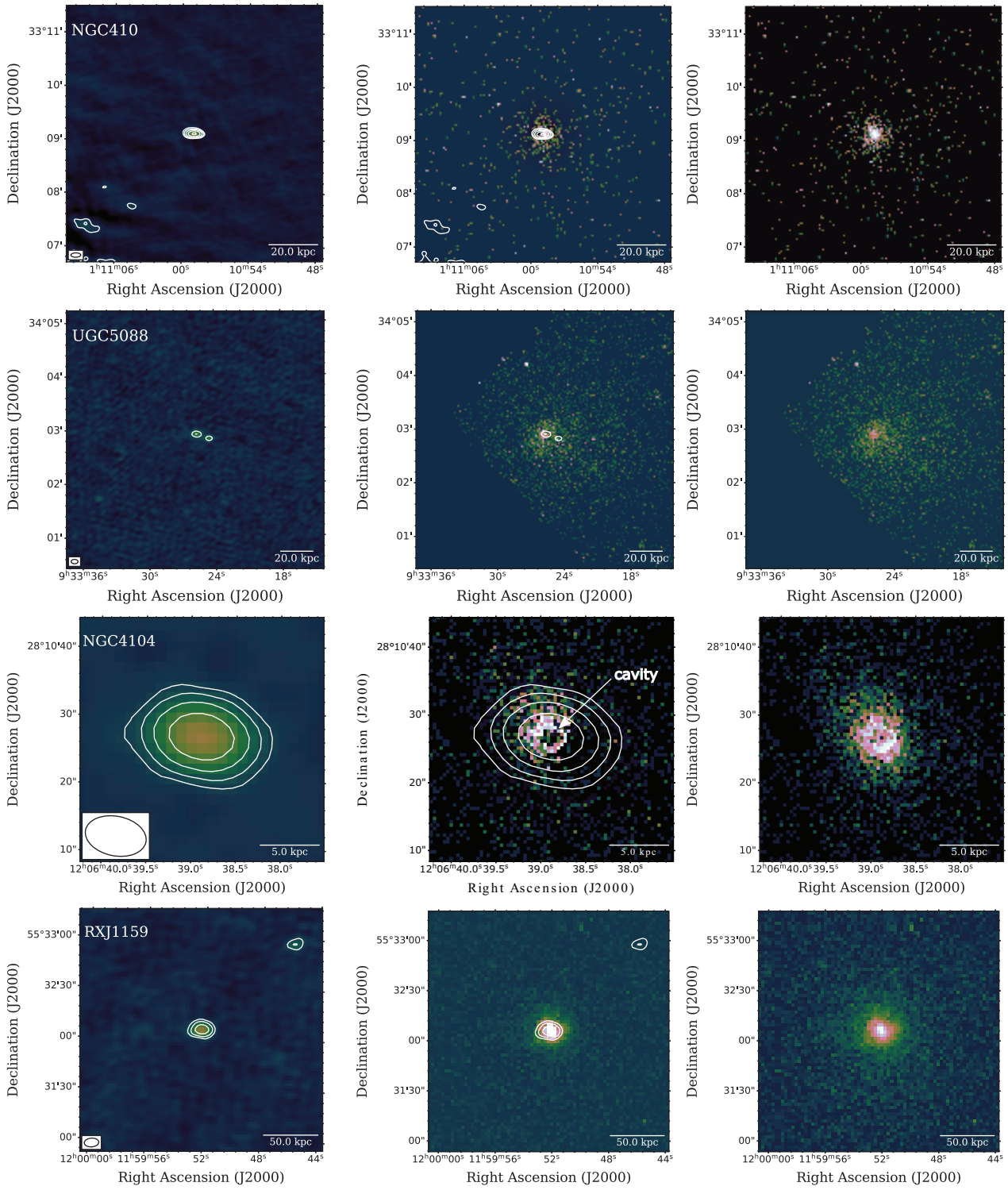

Figure 2. Continued.

The LOFAR and X-ray images for the B08 systems present in our sample are displayed in Fig. 1 (A262), Fig. 3 (A2199, 2A0335+096, A2052, MKW3S, A478, ZwCl 2701, and MS 0735+0721), and Fig. 4 (A1795 and ZwCl 3146). Below, we describe our new observations for the B08 sample:[8]

(i) The LOFAR observation of A262 (see Fig. 1) detected the western lobe at higher significance than previous VLA and GMRT observations (e.g. 327 MHz VLA and 610 MHz GMRT; Bîrzan et al. 2008; Clarke et al. 2009). The full extent of the eastern lobe, as seen by LOFAR, is similar to that seen in the previous observations (e.g. VLA and GMRT).

(ii) The LOFAR observation of 2A0335+096 (see Fig. 3) is significantly more sensitive than previous VLA images (Bîrzan et al.

[8]For more references of the presence of the X-ray cavities see Table 1 and more references for the presence of the central radio source see Table 2.

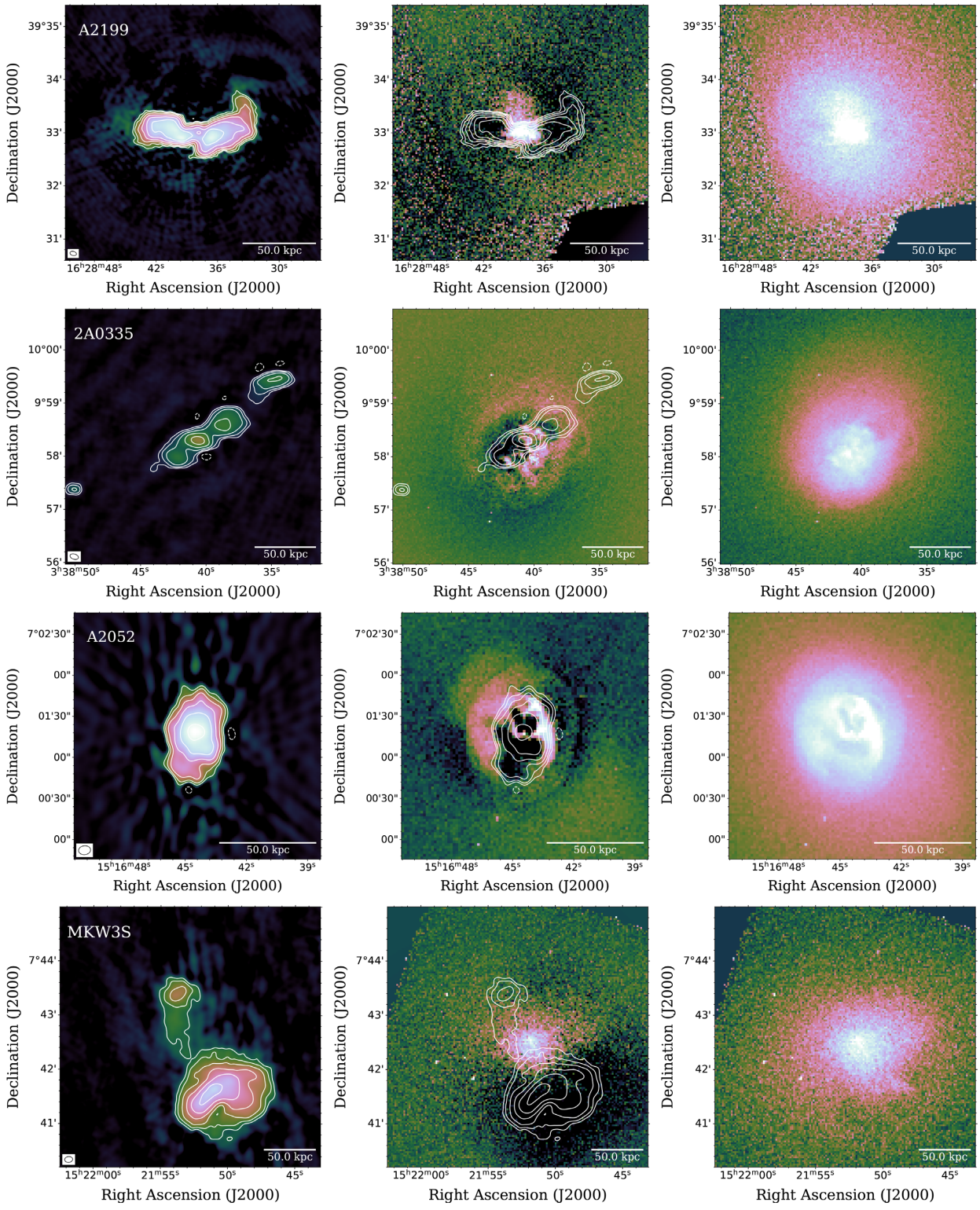

Figure 3. *Chandra* and LOFAR images for the nearby clusters ($z < 0.3$) with X-ray cavities shown in the same order as in Tables 1–3 (A2199, 2A 0335+096, A2052, and MKW3S are shown above, A1668, ZwCl 8276, A478, A1361, ZwCl 0808, ZwCl 2701, MS 0735.6+7421, A2390, and 4C+55.16 are shown in figure continued). The panel organization is the same as in Fig. 1. For the LOFAR image, the first contour is at 0.0285 (A2199), 0.0033 (2A0335+096), 144 (A2052), 0.018 (MKW3S), 0.006 (A1668), 0.0021 (ZwCl 8276), 0.0077 (A478), 0.0587 (A1361), 0.036 (ZwCl 0808), 0.0039 (ZwCl 2701), 0.046 (MS 0735.6+7421), 0.003 57, 0.012 mJy beam^{-1}, and each contour increases by a factor of two.

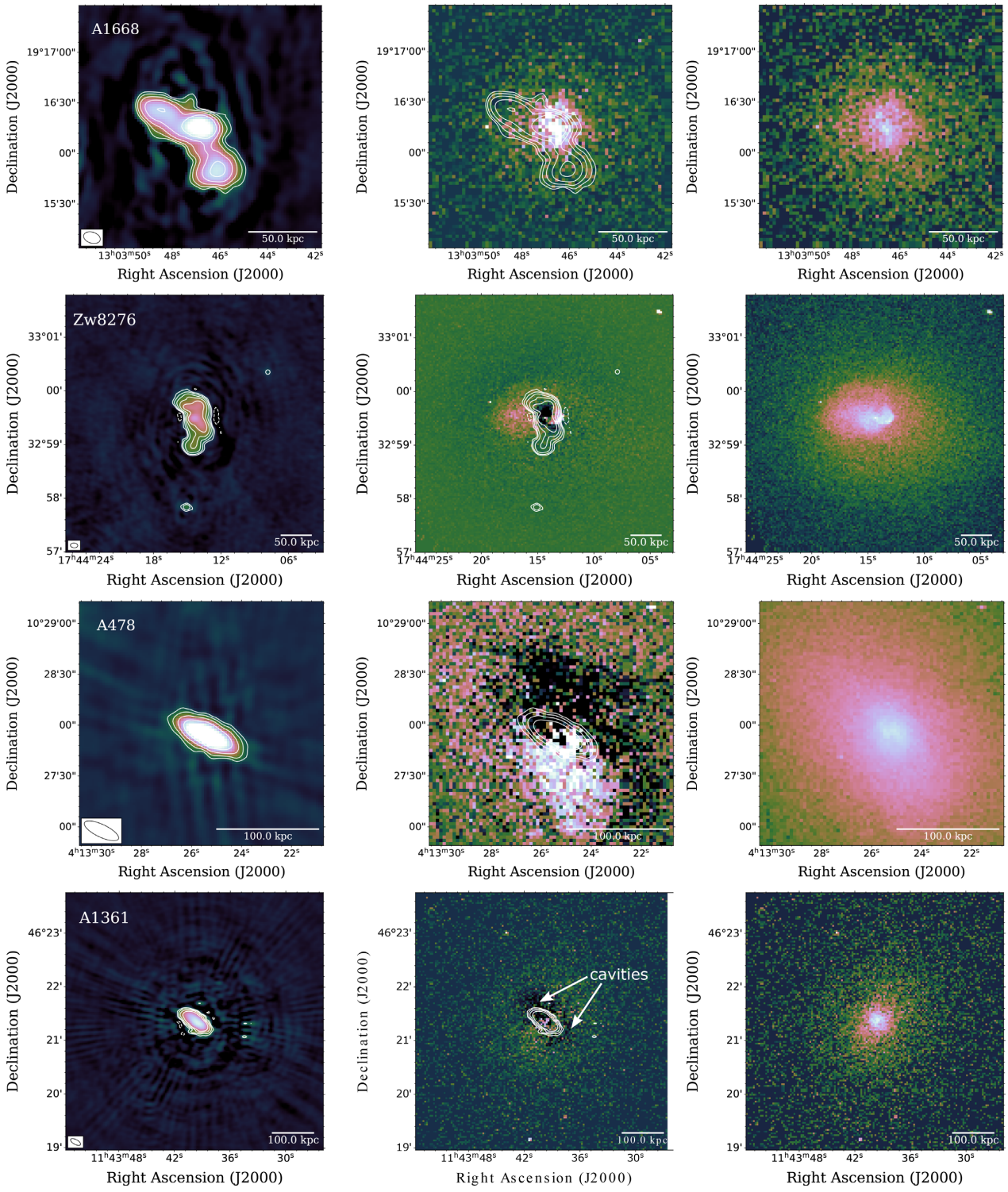

Figure 3. Continued.

2008), where the 327 MHz (B array) and 1.4 GHz (C array) detected only hints of the lobes. In the LOFAR image the lobes are clearly seen, with the north lobe filling in the X-ray cavity visible in the *Chandra* image.[9]

[9]The emission seen beyond the western lobe to the north-west is due to a head-tail radio galaxy seen in previous VLA images.

(iii) The LOFAR observation of ZwCl 2701 (see Fig. 3) shows that lobe emission likely fills the X-ray cavities, in contrast to the previous VLA images (Bîrzan et al. 2008) where we did not detect any lobe emission.

(iv) The LOFAR image for ZwCl 3146 (see Fig. 4) shows for the first time a central radio source with well-resolved lobes. The X-ray residual image shows spiral structure probably created by gas sloshing (see the references in Table 3, e.g. Forman et al. 2002a),

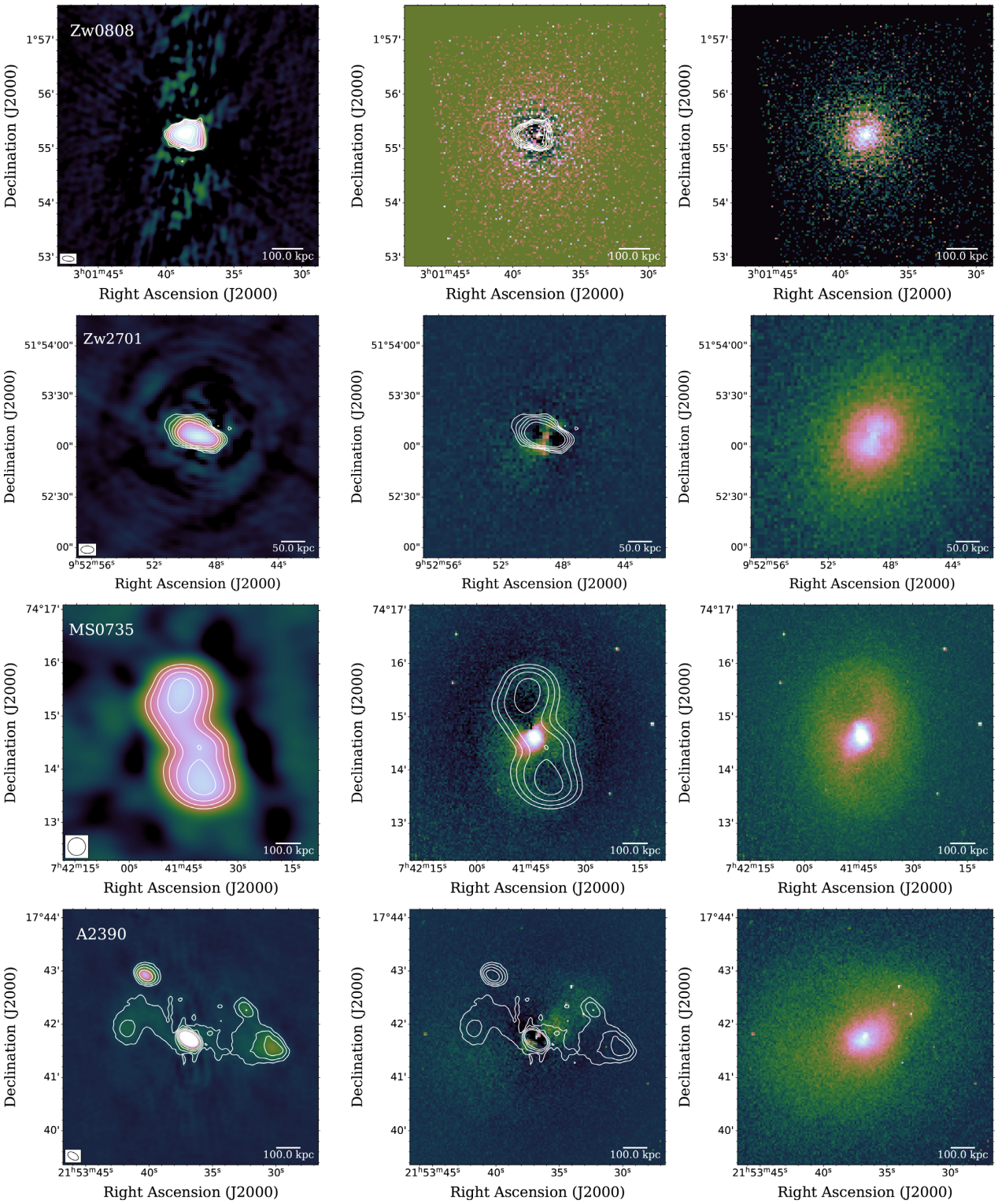

Figure 3. Continued.

which suggests that the cluster may be going through a minor merger (see ZuHone et al. 2010; Zuhone & Roediger 2016). Additionally, there is no direct evidence of cavities at the lobe locations. Because of the complexity of the X-ray morphology we do not include this system in our follow-up cavity sample.

(v) In the case of A1795 there is no apparent association between the central radio source and the large NW cavity which is further out (Walker, Fabian & Kosec 2014): the central radio source is extended NE–SW, the same orientation as the emission seen at higher resolution with the VLA at 1.4 GHz (Ge & Owen 1993; Bîrzan et al. 2008). Our result is consistent with previous GMRT observation from Kokotanekov et al. (2018). Since the central radio source and the X-ray cavity appear to have no association, we will not consider this system in our final cavity sample (for more discussion see Kokotanekov et al. 2018).

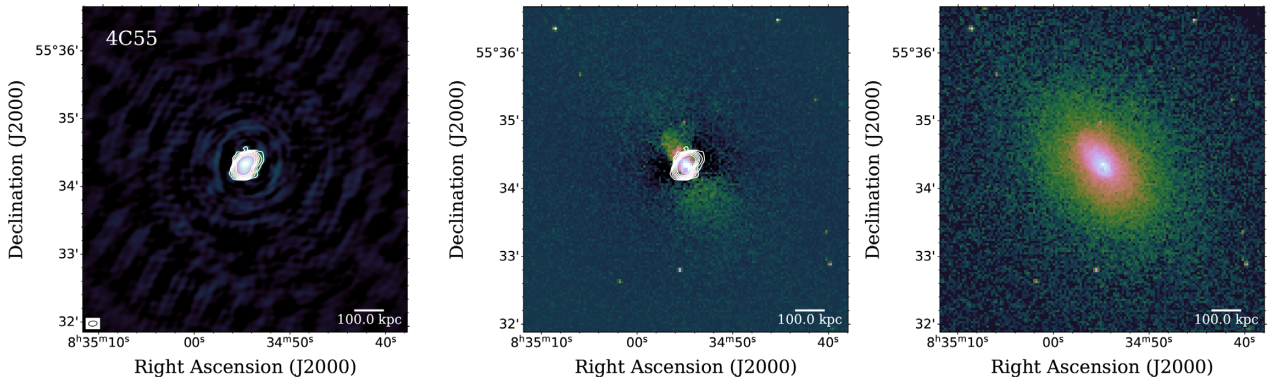

Figure 3. Continued.

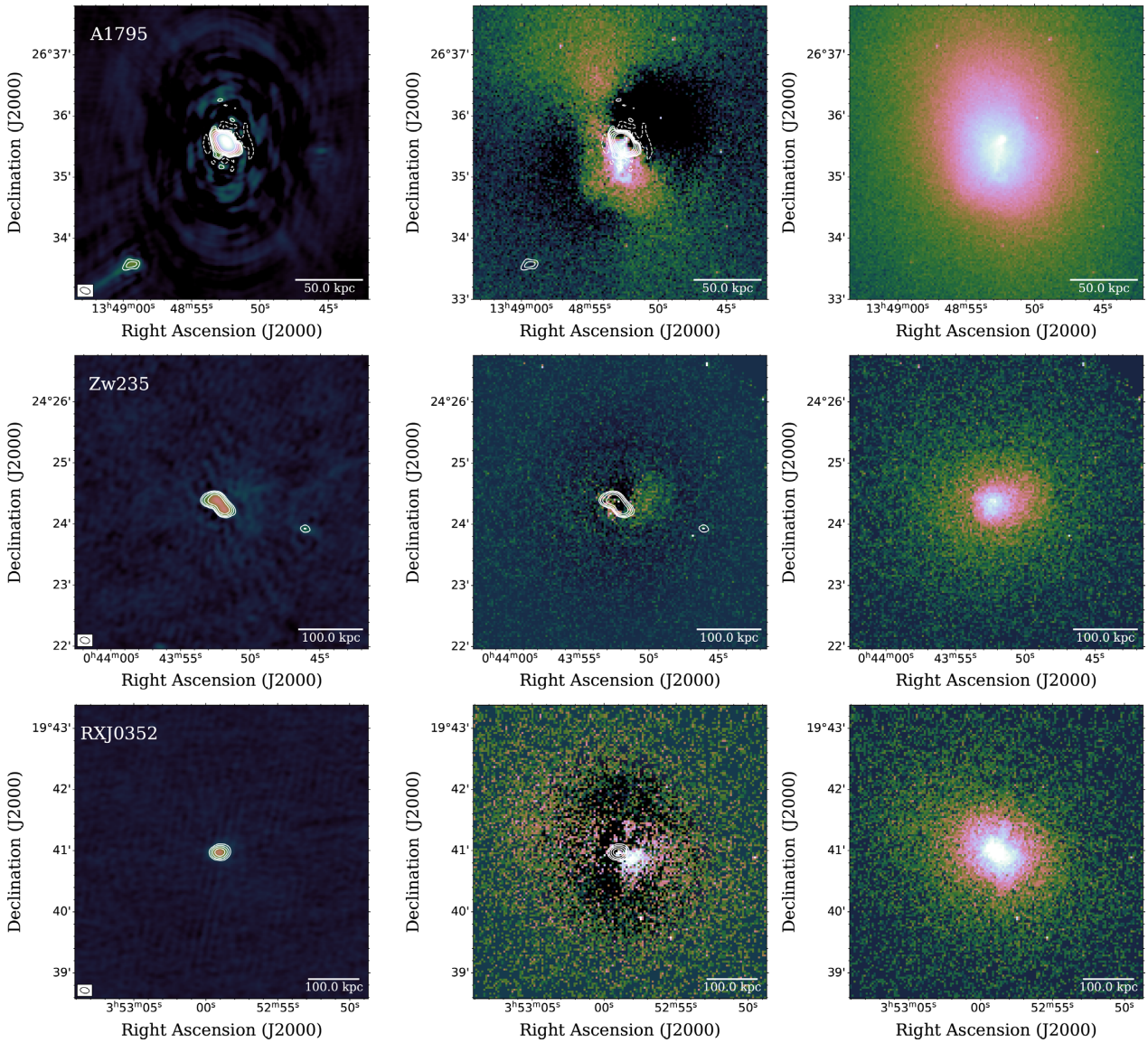

Figure 4. *Chandra* and LOFAR images for the nearby clusters ($z < 0.3$) with X-ray cavities which are not filled with low-frequency radio emission in the same order as in Tables 1–3. The panel organization is the same as in Fig. 1. Shown here are A1795, ZwCl 0235, and RX J0352.9+1941, RX J0820.9+0752, MS 0839.9+2938, and ZwCl 3146 shown in figure continued. For the LOFAR image, the first contour is at 0.018 (A1795; the dashed contour is at −0.018 mJy beam^{-1}), 0.00267 (ZwCl 0235), 0.00267 (RX J0352.9+1941), 0.006 (RX J0820.9+0752), 0.00225 (MS 0839.9+2938), 0.0057 mJy beam^{-1} (ZwCl 3146, the dashed contour is at −0.0057 mJy beam^{-1}), and each contour increases by a factor of two.

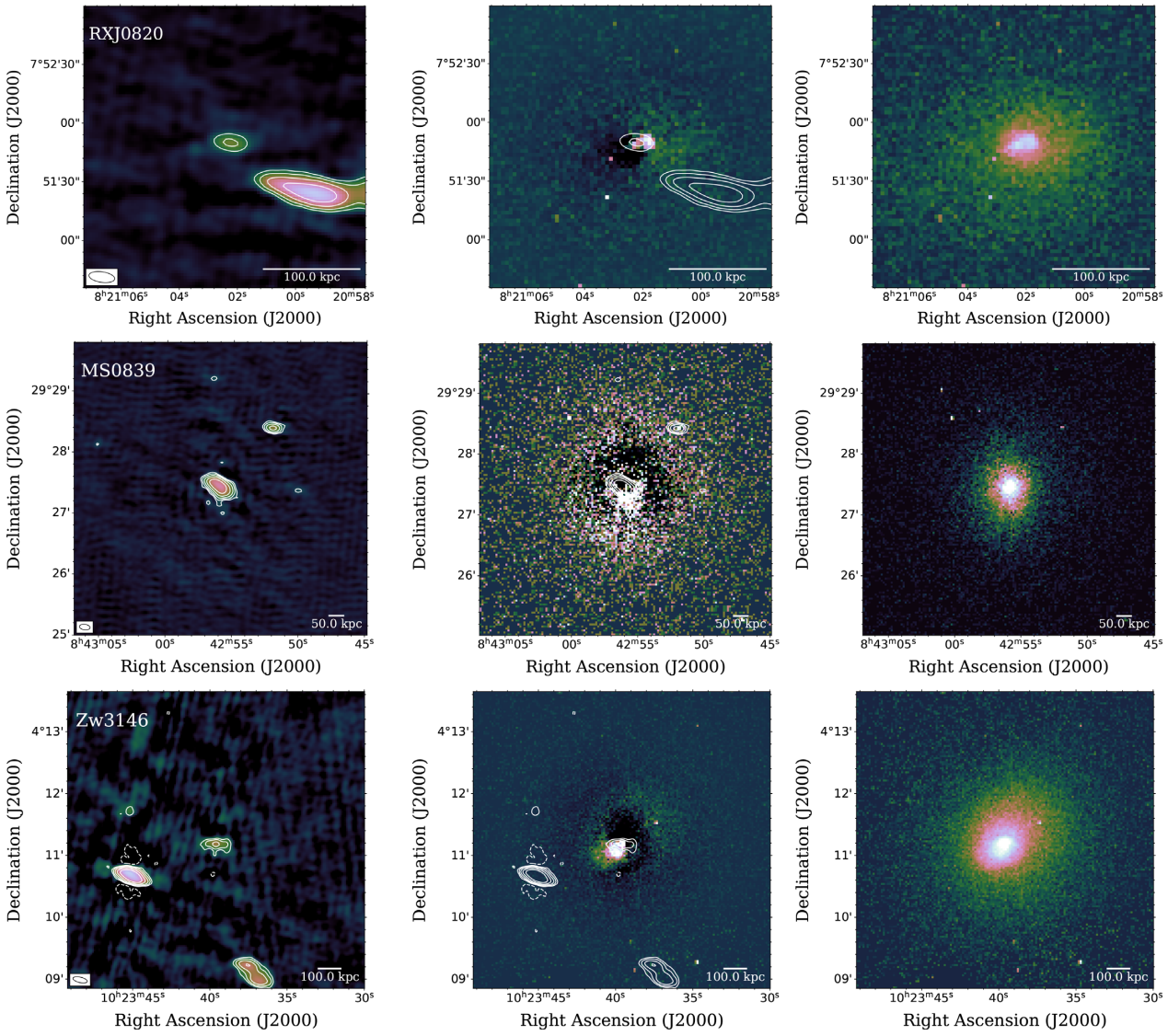

Figure 4. Continued.

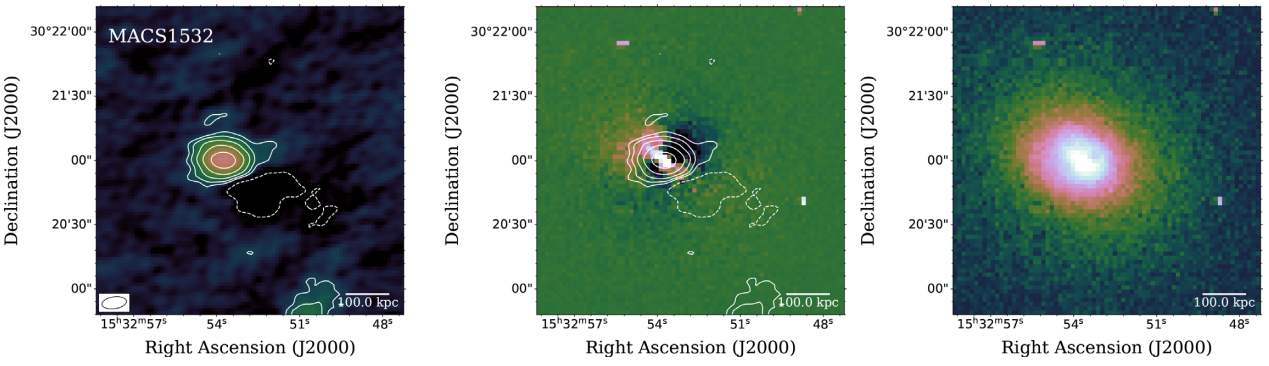

Figure 5. *Chandra* and LOFAR images for the high redshift clusters ($z > 0.3$) with X-ray cavities that are filled with low-frequency radio emission, in the same order as in the tables (with MACS J1532.9+3021 shown above, IRAS 09104+4109 and MACS J1621.3+3810 shown in figure continued). The panel organization is the same as in Fig. 1. For the LOFAR image, the first contour is at 0.0021 (the dashed contour is at −0.0021 mJy beam^{-1}), 0.002 67^{-1} (IRAS 09104+4109), 0.001 95 mJy beam^{-1} (MACS J1621.3+3810), and each contour increases by a factor of two.

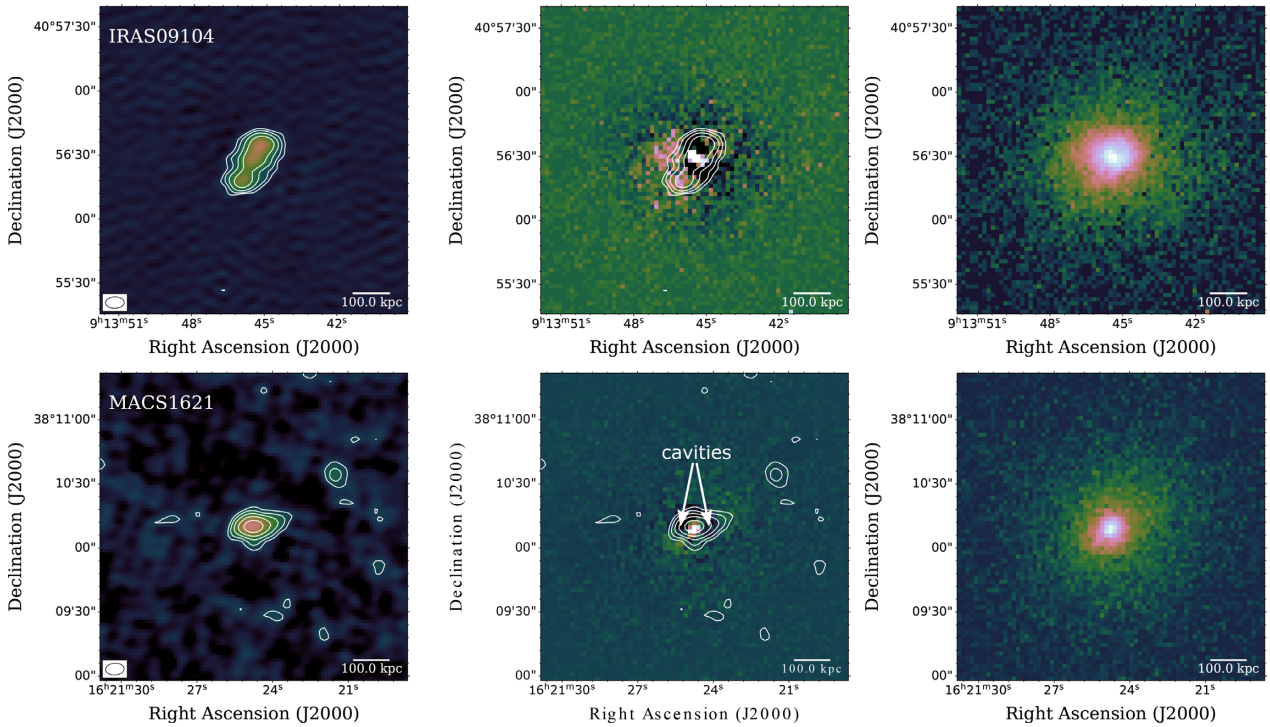

Figure 5. Continued.

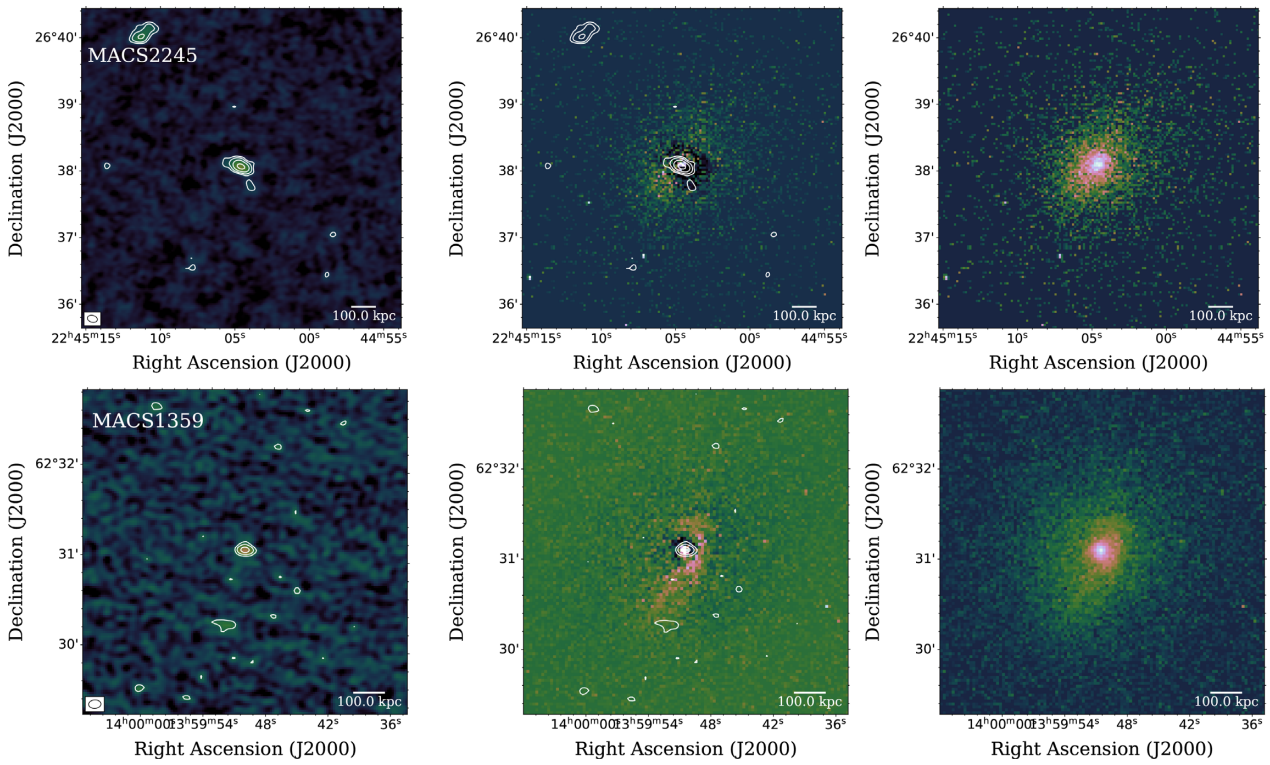

Figure 6. *Chandra* and LOFAR images for the high-redshift clusters ($z > 0.3$) with putative X-ray cavities that are not filled by radio emission, in the same order as in the tables (with MACS J2245.0+2637 and MACS J1359.8+6231 shown above, MACS J1720.2+3536 is shown in figure continued). The panel organization is the same as in Fig. 1. For the LOFAR image, the first contour is at 0.00177 (MACS J2245.0+2637), 0.00096 (MACS J1359.8+6231), 0.006 mJy beam^{-1}, and each contour increases by a factor of two.

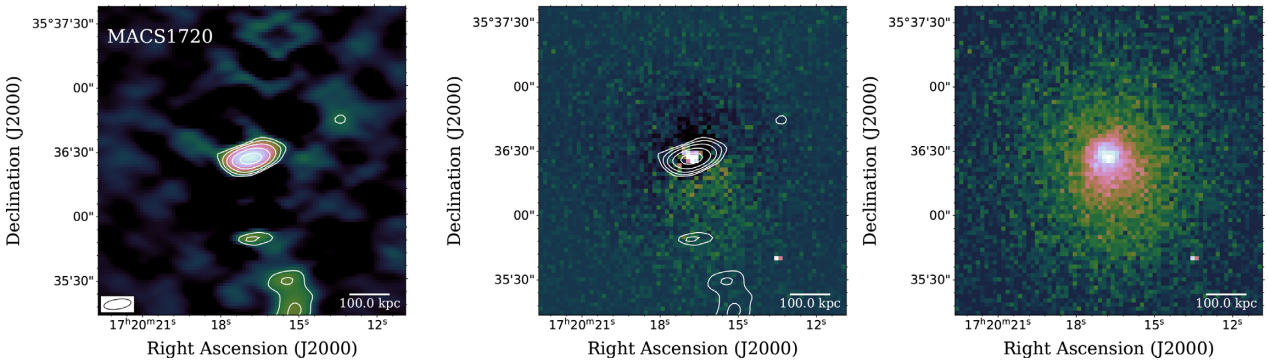

Figure 6. Continued.

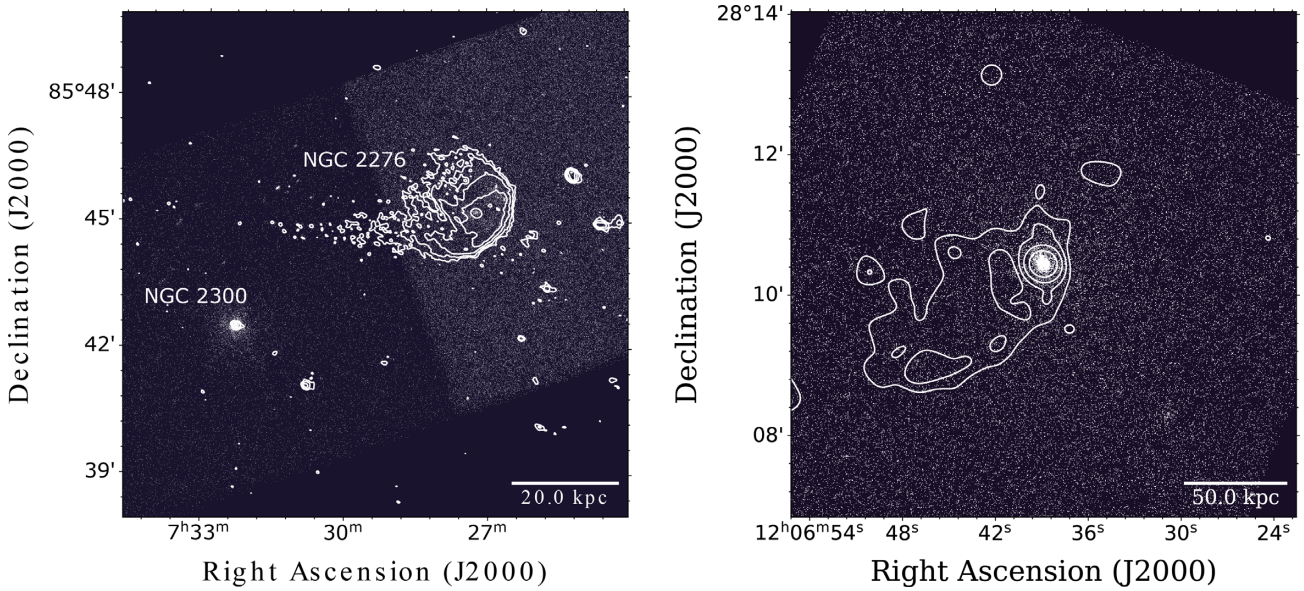

Figure 7. *Left-hand panel*: Overlay of LOFAR contours on the *Chandra* X-ray image, showing together NGC 2300 and NGC 2276. For the LOFAR image, the first contour is at 0.00075mJy beam $^{-1}$, and each contour increases by a factor of two. *Right-hand panel*: Overlay of LOFAR contours of the diffuse emission on the *Chandra* X-ray image in NGC 4104, where the first contour is at 0.0002mJy beam $^{-1}$, and each contour increases by a factor of two.

(vi) The LOFAR image of A478 is from Savini et al. (2019) and does not resolve the small scales of the X-ray cavities as the previous VLA observation does (e.g. VLA at 1.4 GHz, A array; Bîrzan et al. 2008).

(vii) The LOFAR observations of A2199, A2052, and MS 0735.6+7421 (Fig. 3) show resolved central radio sources that fill the X-ray cavities, similar to previous VLA observations (Bîrzan et al. 2008).

(viii) The LOFAR observation of MKW3S (see Fig. 3) detects the emission seen with the VLA and GMRT (Mazzotta et al. 2002; Giacintucci et al. 2007; Bîrzan et al. 2008). For the southern lobe there is a corresponding X-ray cavity in the *Chandra* image, but no corresponding X-ray cavity for the northern lobe has been identified (see Mazzotta et al. 2002; Bîrzan et al. 2004; Dunn & Fabian 2004; Rafferty et al. 2006).

4.2 Groups and ellipticals sample

In the groups and ellipticals sample, besides A262 (see Fig. 1) that is part of the B08 sample, there are other clear cavity systems (we list them in the same order as in Table 1–3)

(i) For NGC 5846, X-ray cavities are reported in Dunn et al. (2010) and Machacek et al. (2011), and radio images at multiple frequencies have been published for this system (see the references in Table 3): from VLA data at 5 and 1.4 GHz (Machacek et al. 2011) and GMRT data at 610 MHz (Giacintucci et al. 2011). The LOFAR observation of NGC 5846 detects the central radio source, but because of the low declination of this source ($\delta_{2000} \sim +01°$), the sensitivity of the observation is quite low.

(ii) For NGC 5813, X-ray cavities are reported in Randall et al. (2015). As with NGC 5846, because of the low declination of the source ($\delta_{2000} \sim +01°$), the sensitivity of the LOFAR observation is quite low. As a result, the LOFAR image detects only emission associated with the inner lobes, whereas previous 235 MHz GMRT observations show radio emission associated with both the inner and outer cavities (Giacintucci et al. 2011).

(iii) NGC 193 has clear X-ray cavities, as presented in Bogdán et al. (2014). The radio lobes, seen also with LOFAR, were imaged previously with the VLA (Laing et al. 2011) and GMRT (Giacintucci et al. 2011). However, the radio-cavity association is complex, and there might be two generations of AGN outbursts (see Bogdán et al. 2014).

(iv) NGC 6338 is an interesting system that is undergoing a merger and has possible cavities (Pandge et al. 2012; O'Sullivan et al. 2019; Wang et al. 2019). Previous radio observations at 1.4 GHz (O'Sullivan et al. 2019; Wang et al. 2019) did not reveal the large lobes seen with LOFAR. These lobes are spatially coincident with the Hα emission (see Pandge et al. 2012), as if the radio lobes dragged the cold gas further in the cluster atmosphere (see McNamara et al. 2016). In a reasonably deep *Chandra* observation (∼300 ks), there is some evidence of an X-ray cavity at the location of the eastern lobe (O'Sullivan et al. 2019), but not at that of the western lobe.

(v) Another spectacular elliptical in our sample is IC1262, with clear X-ray cavities in the *Chandra* image (Dong et al. 2010; Pandge et al. 2019) filled by the radio emission. The two large radio lobes seen in the LOFAR image were reported first in Rudnick & Lemmerman (2009), in WENSS images at 327 MHz, and more recently by Pandge et al. (2019), who used GMRT observations at 325 MHz. Additionally, Pandge et al. (2019) used VLA observations at 1.4 GHz to image the inner lobes of the central radio source, which appear to fill the inner X-ray cavities. They also reported that the outer lobes (seen in our LOFAR observations) have a steep spectral index and that the southern lobe fills a ghost cavity visible in the *Chandra* image. However, there is no visible X-ray cavity associated with the northern lobe (as is also the case in MKW3S). Lastly, Pandge et al. (2019) reported the presence of a phoenix radio source embedded in the southern lobe. This phoenix emission is also visible in the LOFAR image.

(vi) In the case of NGC 6269, the *Chandra* image does not show clear X-ray cavities,[10] but there is a central radio source with well-resolved lobes in the LOFAR image, with structure on a similar scale as other radio observations taken previously (VLA 1.4 GHz and GMRT 235 MHz; Baldi et al. 2009; Giacintucci et al. 2011).

(vii) NGC 5098 has clear X-ray cavities and 1.4 GHz radio emission associated with them (see Randall et al. 2009). The LOFAR image resolves the radio lobes on scales similar to the VLA image.

Among the remaining groups and ellipticals, NGC 741 is a complicated system, where the radio emission observed with LOFAR, and previously with the VLA and GMRT (Jetha et al. 2008; Giacintucci et al. 2011), is probably associated with the nearby galaxy NGC 742, with which NGC 741 is undergoing a merger. However, for NGC 3608 and NGC 777 from Cavagnolo et al. (2010), NGC 2300, UGC 5088, and RX J1159.8+5531 from Dong et al. (2010), NGC 4104 from Shin et al. (2016), and NGC 499 and NGC 410, the LOFAR observations do not detect any lobe emission that fill the reported X-ray cavities. Additionally, NGC 2300 might be merging with the nearby galaxy NGC 2276. The LOFAR image shows that the spiral-shaped radio emission due to SF activity in NGC 2276 extends towards NGC 2300 (see *left-hand* panel of Fig. 7). In the case of NGC 4104 the putative X-ray cavity reported in Shin et al. (2016) is centred on the X-ray core (see Fig. 2), which also corresponds to the core of the BCG, a very unusual location for an AGN cavity, since most AGN cavities are located at a distance of approximately two cavity radii from the core. The LOFAR image detects a central radio source, but does not resolve any lobe emission. Furthermore, NGC 4104 shows diffuse emission on scale of ∼100 kpc (see *right-hand* panel of Fig. 7), which could be an old AGN lobe from a previous AGN outburst. This emission will be investigated in an upcoming paper.

[10]The putative cavities in NGC 6269 are graded as 'C' in Cavagnolo et al. (2010); but the X-ray data are not sufficiently deep for a detailed analysis (see also Baldi et al. 2009).

4.3 Nearby clusters sample ($z < 0.3$)

In this section, we elaborate on the nearby cluster category ($z < 0.3$) that are not present in B08 sample (in the same order as they are listed in Tables 1– 3):

(i) The LOFAR image of A1668 shows large radio lobes that extend far into the ICM (see also Hogan et al. 2015), but the X-ray image is not deep enough to confirm the presence of X-ray cavities coincident with the lobes.

(ii) In the case of ZwCl 8276, the LOFAR image shows a well-resolved central radio source that fills in the cavities reported by Ettori et al. (2013). On the other hand, previous VLA 1.4 GHz DnA-array radio observations from Giacintucci et al. (2014) did not resolve the lobes (e.g. beam size 10.7 arcsec × 9.7 arcsec), and as a result the nature of the extended emission was unclear at that time.

(iii) For A1361, the *Chandra* data were severely affected by flares and only 1.0 ks out of the initial 8.33 ks were used to make the image in Fig. 3. The X-ray residual map image shows some evidence of depressions at the location of the radio lobes, but deeper *Chandra* data would be needed to confirm them. This source was previously imaged with VLA, A array at 1.4 GHz (Owen & Ledlow 1997), and 4.5 GHz (Hogan et al. 2015), which show a two-sided lobe morphology.

(iv) For ZwCl 0808 there is no clear evidence for X-ray cavities at the location of the extended radio emission (see also Hogan et al. 2015), but this has to be further confirmed with deeper *Chandra* data.

(v) For A2390, the presence of X-ray cavities was reported by Sonkamble et al. (2015) and Shin et al. (2016). However, it was not until the LOFAR observations of Savini et al. (2019) that a central radio source with large lobes was detected.[11] A2390 is a good example of the lobes of the central radio source filling the X-ray cavities.

(vi) For 4C+55.16, LOFAR confirms the presence of radio emission filling the X-ray cavities (e.g. Xu et al. 1995; Rafferty et al. 2006; Hlavacek-Larrondo et al. 2011).

Next, based on our LOFAR observations, we discuss the systems where the X-ray cavities reported in the literature are not filled with radio emission (the systems are presented in the same order as in Tables 1–3):

(i) LOFAR observation of ZwCl 0235 (see Fig. 4) shows a central radio source with small lobes associated with the BCG. However, there are no evident X-ray cavities at the lobe location.[12] This source might be similar to ZwCl 3146, since shows clear evidence for a spiral residual pattern in the ICM, often found to be associated with sloshing (see ZuHone et al. 2010).

(ii) LOFAR image of RX J0352.9+1941 shows a point-like central radio source, associated with the BCG. As in the case of ZwCl 0235 (see footnote) putative X-ray cavities were reported in the literature by Shin et al. (2016). However, there does not seem

[11]The LOFAR image of A2390 used in this paper is from Savini et al. (2019).
[12]For ZwCl 0235 there were putative cavities reported in the literature (Shin et al. 2016). However, we do not know the size and location of these reported cavities.

to be any clear X-ray depression in this system and no central radio source with lobes either.

(iii) For RX J0820.9+0752, the LOFAR image does not show radio lobes filling the putative X-ray cavity (Vantyghem et al. 2019). The reported cavity is larger and further out in the ICM than the location of the central radio source imaged with LOFAR (Vantyghem et al. 2019).

(iv) The LOFAR image of MS 0839.9+2938 confirms the presence of a central radio source with small lobes, previously reported by Giacintucci et al. (2017) using VLA B and C arrays at 1.4 GHz. However, there are no clear corresponding X-ray cavities at the location of the lobes. Low-significance cavities were reported by Shin et al. (2016), but we do not know their size and location relative to the radio lobes seen in the LOFAR image.

4.4 High-redshift clusters sample ($z > 0.3$)

In the high-redshift sample, there are two clear cavity systems and one possible cavity system:

(i) For MACS J1532.9+3021, where the X-ray cavities are reported in Hlavacek-Larrondo et al. (2012, 2013a), LOFAR did not resolve the lobes. The interpretation in the literature is that the radio emission is a mini-halo (see Kale et al. 2013; Hlavacek-Larrondo et al. 2013a; Giacintucci et al. 2014).

(ii) For IRAS 09104+4109, X-ray cavities were reported in O'Sullivan et al. (2012) and Hlavacek-Larrondo et al. (2012). The morphology of the radio emission in the LOFAR image is similar to the GMRT and VLA images presented in O'Sullivan et al. (2012).

(iii) MACS J1621.3+3810 was previously imaged at 365 MHz as part of WENSS, the Westerbork Northern Sky Survey (see Edge et al. 2003). The LOFAR image shows an extended central radio source, but better resolution is required to resolve any lobes.

For the remaining higher redshift systems, MACS J2245.0+2637, MACS J1359.8+6231, and MACS J1720.2+3536, there is no detected LOFAR radio emission in the X-ray cavities reported in Hlavacek-Larrondo et al. (2012). In these systems, the reported cavities are far beyond the extent of the central radio sources imaged with LOFAR. On a much smaller scale than the cavities reported in Hlavacek-Larrondo et al. (2012), there might be hints of lobe emission for the central radio source in MACS J2245.0+263; however, the source is not well resolved in the present LOFAR images.[13]

5 DISCUSSION

This work presents LOFAR HBA observations at 143 MHz for a sample of clusters, groups, and ellipticals with previously reported X-ray cavities. We separated the sample into three subsamples: groups and ellipticals, nearby ($z < 0.3$) clusters, and higher redshift ($z > 0.3$) clusters.

[13]In many of the higher redshift systems, use of the LOFAR international stations will be required to achieve the arcsecond resolution needed to resolve any emission in the cavities identified in the X-ray images, as the size of the cavities is below the LOFAR resolution limit when international stations are not used. The development of techniques to use the international stations is a work in progress (e.g. Varenius et al. 2015, 2016; Morabito 2016).

5.1 Group and ellipticals subsample

For the group and elliptical subsample, in addition to A262 that was present in B08, we observed candidate cavity systems from Cavagnolo et al. (2010), O'Sullivan et al. (2011), and Dong et al. (2010). We found that only 6 out of 17 systems are good AGN feedback candidates (see Table 3), and the two best cavity systems, NGC 5813 and NGC 5846, unfortunately have relatively low-radio flux densities and are located at $\delta_{2000} \approx +0°$. Therefore, the sensitivity of the LOFAR observations of these systems is not sufficient to image the full extent of the radio lobes. For NGC 6338, the LOFAR observations reveal previously unknown extended emission, with the eastern lobe being coincident with a putative X-ray cavity (O'Sullivan et al. 2019).

In 9 of the 17 group and elliptical cavity system candidates we did not detect lobes (e.g. NGC 777, NGC 3608, and NGC 2300), so the construction of a sample of radio-filled cavities systems in the groups and ellipticals category has been so far a difficult problem. Additionally, in X-rays the study of AGN feedback in group and ellipticals is limited by *Chandra's* capability to image the diffuse gas in such systems. Nevertheless, although we do not have a large sample from which to draw firm conclusions, the established picture is expected to hold, in which mechanical AGN feedback in elliptical galaxies is less powerful and efficient than in clusters (Gaspari, Brighenti & Temi 2012), with an average duty cycle of $\sim 1/3$ (O'Sullivan et al. 2017). The duty cycle may increase with the size of the system (Nulsen et al. 2009), and generally the reservoir of cold gas has a major influence in the AGN feedback process (Gaspari et al. 2012; Li & Bryan 2014b; Valentini & Brighenti 2015). Additionally, another complication with the lower X-ray luminosity systems is that one cannot assume that any undetected X-ray cavities are well traced by the radio lobes, since such systems often host high-power radio sources whose lobes extend far beyond the dense atmospheres (e.g. NGC 4261, IC4296, IC1459, NGC 1600, NGC 5090, UGC11294, ARP308; Diehl & Statler 2008; Sun 2009; Cavagnolo et al. 2010; Duţan & Caramete 2015; Kolokythas et al. 2018; Ruffa et al. 2019; Grossová et al. 2019).

Table 3 shows that H α filaments are mostly found in groups and ellipticals where the radio emission is filling the X-ray cavities (the exceptions are NGC 499, NGC 410, and NGC 4104, see Table 3). This result is broadly consistent with the study of Lakhchaura et al. (2018), where in a sample of 49 nearby elliptical galaxies they found a hint of a trend between the presence of H α emission and the AGN jet power (see also Babyk et al. 2019).

5.2 Nearby and higher redshift cluster subsamples

For the nearby cluster sample, our LOFAR observations have sufficient sensitivity and spatial resolution to detect the radio lobes present at the centre of most nearby cooling flow clusters (for 17 out of 19 systems we detected radio lobes, the exceptions being RX J0352.9+1941 and RX J0820.9+0752). In some such systems with known X-ray cavities, e.g. 2A0335+096 (Mazzotta, Edge & Markevitch 2003), ZwCl 2701 (Rafferty et al. 2006), and ZwCl 8276 (Ettori et al. 2013), the cavity-radio association was not clear from previous radio images. The LOFAR observations of these systems show us that the X-ray cavities are indeed filled with low-frequency radio emission.

On the other hand, the LOFAR images of A1795, ZwCl 3146, and ZwCl 235 do not show diffuse radio emission[14] associated with the cavities (Rafferty et al. 2006; Shin et al. 2016; Kokotanekov et al. 2018), and as a result the nature of the cavities is still unclear. In particular, A1795, besides showing evidence for sloshing activity (see Table 3 for references, Ghizzardi, Rossetti & Molendi 2010), may be going through a merging process, with the Hα filaments (Crawford, Sanders & Fabian 2005; McDonald & Veilleux 2009; Mittal, Whelan & Combes 2015; Tremblay et al. 2015) being dragged along by the 'flying' cluster core (Ehlert et al. 2015). Furthermore, RX J0352.9+1941 and RX J0820.9+0752 do not have lobe-like central radio emission, and as a result we cannot confirm a X-ray/radio association (Shin et al. 2016; Vantyghem et al. 2019), but they do show Hα filaments and molecular gas (Bayer-Kim et al. 2002; Hamer et al. 2016; Vantyghem et al. 2019).

In addition to the AGN heating trough X-ray cavities, the ICM heating can occur through other means, e.g. uplifting of the cold gas from the centre of the cluster through sloshing motions (e.g. Fornax cluster, A1068; Su et al. 2017; McNamara, Wise & Murray 2004), by the central radio source and/or radio bubbles (Peterson & Fabian 2006; Revaz et al. 2008; Kirkpatrick & McNamara 2015; Hamer et al. 2016; McNamara et al. 2016), by the flying cluster core (e.g. A1795, Crawford et al. 2005; Ehlert et al. 2015) or even by major merger with another cluster or subcluster (e.g. A2146; Canning et al. 2012).[15] Also, all nearby cooling flow systems, regardless of whether or not they have X-ray cavities, show evidence of sloshing activity and possess Hα filaments (see Table 3), as if the heating done by cavities and sloshing goes together in some cases (e.g. Fornax Cluster, Perseus; Su et al. 2017; Walker, Sanders & Fabian 2018). It would be important to understand if such heating is more critical for the cooling flow clusters without cavities and without a central radio source with lobes (e.g. A1068).

Additionally, some systems in our sample are likely in a cooling stage. We know from studying complete samples that the duty cycle of radio-mode feedback is ≈ 70 per cent (Bîrzan et al. 2012) and that the cooling stage is not always clearly separated from the heating stage. Also, the detectability of a cavity depends on its location, orientation, angular size, and the depth of the X-ray observations (Enßlin & Heinz 2002; Diehl et al. 2008; Brüggen, Scannapieco & Heinz 2009). Also, it is important to note that there is an evolution to any X-ray cavity and we will tend to observe X-ray cavities in only a fraction of clusters where the system is in the middle stage of the cycle with well inflated cavities that are well filled with the energetic electrons (the lobes seen in radio). As a result, some systems might be in the early stages of their current activity, and what we see in LOFAR images might be from previous radio activity (e.g. A2390).

Our LOFAR observations generally show that the low-frequency radio-emitting plasma does not appear to extend much beyond the cavity edges, e.g. in MS 0735.6+7421 and A2052 (see also M87, de Gasperin et al. 2012). This finding has important implications for simulations of the X-ray cavities, such as the interaction of radio lobes with the ICM and the magnetic field configuration inside the cavities (see Pfrommer 2013). Observationally, it was found that the energy content of the cavities is not dominated by the radio-emitting electrons (e.g. Morganti et al. 1988; Dunn & Fabian 2004; Bîrzan et al. 2008; Croston et al. 2008; Croston, Ineson & Hardcastle 2018), and there are observational constraints on the amount of hot gas filling the cavities (Abdulla et al. 2019). As a result, the most promising candidate for pressure support of the cavities is CR protons. There are some constraints on the confinement time of CR protons from the non-detection with γ-ray telescopes (Prokhorov & Churazov 2017). There are also a large number of simulations that investigate the heating of the ICM with CRs (Guo & Oh 2008; Sharma, Parrish & Quataert 2010; Pfrommer 2013; Wiener, Oh & Guo 2013; Ruszkowski et al. 2017; Weinberger et al. 2017; Ehlert et al. 2018; Thomas & Pfrommer 2019; Yang, Gaspari & Marlow 2019), or by the mixing of the bubble contents, which can be either hot gas and/or CR protons, with the ICM. The latter process is thought to happen at the bubble surface through vortices (Brüggen & Kaiser 2002; Brüggen et al. 2009; Yang & Reynolds 2016; Hillel & Soker 2017). Also, the cavities could have pressure support from very hot thermal plasma, for example in the case of Perseus, half of the cavity volume could be filled with 50 keV thermal gas (Sanders & Fabian 2007).

However, not all the X-ray cavities are as well defined as in A2052 or MS 0735.6+7421. But, the LOFAR observations show that, in the case of nearby clusters, the radio lobes generally appear to be well confined. Thus, we can postulate that the radio lobes generally fill the X-ray cavities with no major evidence of CR electrons leaking. However, it is important to remember that the interaction of the radio source with these rich and dynamic clusters environments is complicated, since sloshing and other cluster weather is also often present (e.g. in A2199 the western lobe is curved and appears to be moving back in the direction of cluster motion). As a result, the FRI sources that tend to exist in rich cluster environments might be different than the FRI sources that are more common in poor cluster and group environments (see also Croston et al. 2018), since sloshing motions can provide some re-acceleration of the existing electron population (e.g. de Gasperin et al. 2017). Additionally, in the case of nearby and higher redshift clusters, Table 3 shows that, even if the Hα emission is present in systems with and without a good correlation between the X-ray cavities and the lobe radio emission, the systems with cavities filled by the radio lobe emission tend to host more powerful radio sources than those without (see also Hogan et al. 2015).

6 CONCLUSIONS

The goal of this paper is to search for diffuse radio emission at low frequencies in a sample of systems that have possible cavities in X-ray images. To this end, we have imaged a total of 42 such systems with LOFAR, of which 17 are nearby groups and ellipticals, 19 are nearby massive clusters ($z < 0.3$), and 6 are higher redshift clusters ($z > 0.3$).

Based on the presence of low-frequency radio emission that fills the X-ray cavities, we conclude that only 11/19 of the nearby massive clusters show clear evidence for radio mode AGN feedback, where the cavities and the central radio source are well correlated (the associations for A1668 and ZwCl 0808 need to be further confirmed). Additionally, 3/6 high redshift clusters and 7/17 nearby groups and ellipticals show such evidence (NGC 6269 need to be further confirmed; see Table 3). As a result, building a large, statistically significant sample of low-frequency observations of systems with cavities in each of the three categories will require the use of other telescopes (e.g. the VLA and GMRT) to add systems

[14]Lower frequency LOFAR LBA observations might provide further constraints on the presence of even older electron populations.

[15]In some of the nearby and high-redshift clusters there is additional evidence for sloshing motion or minor merging activity, such as a displacement between the X-ray peak, the Hα peak, and the BCG (e.g. Crawford et al. 2005; Ehlert et al. 2015; Hamer et al. 2016; McDonald et al. 2016).

situated at $\delta_{2000} < 0^{\circ}$ and the use of the LOFAR international stations since, generally, the LOFAR observations of systems at higher redshift are limited due to the lack of resolution. In particular, the typical resolution achievable without the international stations (≈5–10 arcsec) implies a limiting physical scale of ∼20–40 kpc at redshifts of ∼0.3, whereas typical cavities observed in such systems have sizes of ∼10–20 kpc, (e.g. RBS 797, MACS J1423.8+2404, and MACS J1532.9+3021, Rafferty et al. 2006; Hlavacek-Larrondo et al. 2013a).

ACKNOWLEDGEMENTS

The scientific results reported in this article are based on data obtained with the International LOFAR Telescope (ILT), and archive data from *Chandra* Data Archive and *XMM–Newton* archive. LOFAR (van Haarlem et al. 2013) is the Low Frequency Array designed and constructed by ASTRON. It has observing, data processing, and data storage facilities in several countries, that are owned by various parties (each with their own funding sources), and that are collectively operated by the ILT foundation under a joint scientific policy. The ILT resources have benefitted from the following recent major funding sources: CNRS-INSU, Observatoire de Paris and Université d'Orléans, France; BMBF, MIWF-NRW, MPG, Germany; Science Foundation Ireland (SFI), Department of Business, Enterprise and Innovation (DBEI), Ireland; NWO, The Netherlands; The Science and Technology Facilities Council, UK. The LOFAR reduction was done using the PREFACTOR and FACTOR packages. The authors thank Federica Savini for providing LOFAR images of A478 and A2390. ACE acknowledges support from STFC grant ST/P00541/1. HR acknowledges support from the ERC Advanced Investigator programme NewClusters 321271. AB acknowledges support from the VIDI research programme with project number 639.042.729, which is financed by the Netherlands Organisation for Scientific Research (NWO). We acknowledge the 'Multiphase AGN Feeding and Feedback' workshop held in Sexten, Italy, on 2018 July, for stimulating discussion. The authors thank the referee for the careful reading of the draft and the comments which improved and clarified the paper.

REFERENCES

Abdulla Z. et al., 2019, ApJ, 871, 195
Alexander D. M., Hickox R. C., 2012, New Astron. Rev., 56, 93
Babyk I. V., McNamara B. R., Tamhane P. D., Nulsen P. E. J., Russell H. R., Edge A. C., 2019, ApJ, 887, 149
Baldi A., Forman W., Jones C., Nulsen P., David L., Kraft R., Simionescu A., 2009, ApJ, 694, 479
Bambic C. J., Morsony B. J., Reynolds C. S., 2018, ApJ, 857, 84
Bayer-Kim C. M., Crawford C. S., Allen S. W., Edge A. C., Fabian A. C., 2002, MNRAS, 337, 938
Best P. N., Kaiser C. R., Heckman T. M., Kauffmann G., 2006, MNRAS, 368, L67
Best P. N., von der Linden A., Kauffmann G., Heckman T. M., Kaiser C. R., 2007, MNRAS, 379, 894
Best P. N., Ker L. M., Simpson C., Rigby E. E., Sabater J., 2014, MNRAS, 445, 955
Bicknell G. V., 1984, ApJ, 286, 68
Bîrzan L., Rafferty D. A., McNamara B. R., Wise M. W., Nulsen P. E. J., 2004, ApJ, 607, 800
Bîrzan L., McNamara B. R., Nulsen P. E. J., Carilli C. L., Wise M. W., 2008, ApJ, 686, 859
Bîrzan L., Rafferty D. A., Nulsen P. E. J., McNamara B. R., Röttgering H. J. A., Wise M. W., Mittal R., 2012, MNRAS, 427, 3468
Bîrzan L., Rafferty D. A., Brüggen M., Intema H. T., 2017, MNRAS, 471, 1766
Bîrzan L. et al., 2019, MNRAS, 487, 4775
Blanton E. L., Sarazin C. L., McNamara B. R., Wise M. W., 2001, ApJ, 558, L15
Blanton E. L., Sarazin C. L., McNamara B. R., 2003, ApJ, 585, 227
Blanton E. L., Sarazin C. L., McNamara B. R., Clarke T. E., 2004, ApJ, 612, 817
Blanton E. L., Randall S. W., Clarke T. E., Sarazin C. L., McNamara B. R., Douglass E. M., McDonald M., 2011, ApJ, 737, 99
Bogdán Á. et al., 2014, ApJ, 782, L19
Brighenti F., Mathews W. G., Temi P., 2015, ApJ, 802, 118
Brüggen M., Kaiser C. R., 2002, Nature, 418, 301
Brüggen M., Scannapieco E., Heinz S., 2009, MNRAS, 395, 2210
Burns J. O., Schwendeman E., White R. A., 1983, ApJ, 271, 575
Canning R. E. A. et al., 2012, MNRAS, 420, 2956
Cappellari M. et al., 2006, MNRAS, 366, 1126
Cattaneo A., Best P. N., 2009, MNRAS, 395, 518
Cattaneo A. et al., 2009, Nature, 460, 213
Cavagnolo K. W., Donahue M., Voit G. M., Sun M., 2008, ApJ, 683, L107
Cavagnolo K. W., McNamara B. R., Nulsen P. E. J., Carilli C. L., Jones C., Bîrzan L., 2010, ApJ, 720, 1066
Churazov E., Sazonov S., Sunyaev R., Forman W., Jones C., Böhringer H., 2005, MNRAS, 363, L91
Clarke T. E., Blanton E. L., Sarazin C. L., Anderson L. D., Gopal-Krishna, Douglass E. M., Kassim N. E., 2009, ApJ, 697, 1481
Crawford C. S., Allen S. W., Ebeling H., Edge A. C., Fabian A. C., 1999, MNRAS, 306, 857
Crawford C. S., Sanders J. S., Fabian A. C., 2005, MNRAS, 361, 17
Croston J. H., Hardcastle M. J., Birkinshaw M., Worrall D. M., Laing R. A., 2008, MNRAS, 386, 1709
Croston J. H., Ineson J., Hardcastle M. J., 2018, MNRAS, 476, 1614
Croton D. J. et al., 2006, MNRAS, 365, 11
Croton D. J. et al., 2016, ApJS, 222, 22
Daly R. A., Sprinkle T. B., O'Dea C. P., Kharb P., Baum S. A., 2012, MNRAS, 423, 2498
Danielson A. L. R., Lehmer B. D., Alexander D. M., Brandt W. N., Luo B., Miller N., Xue Y. Q., Stott J. P., 2012, MNRAS, 422, 494
de Gasperin F. et al., 2012, A&A, 547, A56
de Gasperin F. et al., 2017, Sci. Adv., 3, e1701634
Dekel A., Lapiner S., Dubois Y., 2019, preprint (arXiv:1904.08431)
Diehl S., Statler T. S., 2008, ApJ, 680, 897
Diehl S., Li H., Fryer C. L., Rafferty D., 2008, ApJ, 687, 173
Donahue M., Stocke J. T., Gioia I. M., 1992, ApJ, 385, 49
Donahue M., Sun M., O'Dea C. P., Voit G. M., Cavagnolo K. W., 2007, AJ, 134, 14
Donahue M. et al., 2015, ApJ, 805, 177
Dong R., Rasmussen J., Mulchaey J. S., 2010, ApJ, 712, 883
Dunn R. J. H., Fabian A. C., 2004, MNRAS, 355, 862
Dunn R. J. H., Fabian A. C., Taylor G. B., 2005, MNRAS, 364, 1343
Dunn R. J. H., Fabian A. C., Sanders J. S., 2006, MNRAS, 366, 758
Dunn R. J. H., Allen S. W., Taylor G. B., Shurkin K. F., Gentile G., Fabian A. C., Reynolds C. S., 2010, MNRAS, 404, 180
Duțan I., Caramete L. I., 2015, Astropart. Phys., 62, 206
Edge A. C., Wilman R. J., Johnstone R. M., Crawford C. S., Fabian A. C., Allen S. W., 2002, MNRAS, 337, 49
Edge A. C., Ebeling H., Bremer M., Röttgering H., van Haarlem M. P., Rengelink R., Courtney N. J. D., 2003, MNRAS, 339, 913
Ehlert S., McDonald M., David L. P., Miller E. D., Bautz M. W., 2015, ApJ, 799, 174
Ehlert K., Weinberger R., Pfrommer C., Pakmor R., Springel V., 2018, MNRAS, 481, 2878
Enßlin T. A., Heinz S., 2002, A&A, 384, L27
Ettori S., Gastaldello F., Gitti M., O'Sullivan E., Gaspari M., Brighenti F., David L., Edge A. C., 2013, A&A, 555, A93
Faber S. M. et al., 2007, ApJ, 665, 265
Fabian A. C., 1994, ARA&A, 32, 277
Fabian A. C., 2012, ARA&A, 50, 455

Fabian A. C., Sanders J. S., Allen S. W., Crawford C. S., Iwasawa K., Johnstone R. M., Schmidt R. W., Taylor G. B., 2003, MNRAS, 344, L43
Fabian A. C., Walker S. A., Russell H. R., Pinto C., Sanders J. S., Reynolds C. S., 2017, MNRAS, 464, L1
Fanaroff B. L., Riley J. M., 1974, MNRAS, 167, 31P
Fanti C., Fanti R., de Ruiter H. R., Parma P., 1987, A&AS, 69, 57
Fogarty K., Postman M., Connor T., Donahue M., Moustakas J., 2015, ApJ, 813, 117
Forman W., Jones C., Markevitch M., Vikhlinin A., Churazov E., 2002a, in Gilfanov M., Sunyeav R., Churazov E., eds, Lighthouses of the Universe: The Most Luminous Celestial Objects and Their Use for Cosmology, ESO ASTROPHYSICS SYMPOSIA (European Southern Observatory). Springer, Berlin, Heidelberg, p. 51
Forman W., Jones C., Markevitch M., Vikhlinin A., Churazov E., 2002b, in Celnikier L. M., ed., Contribution to XIII Rencontres de Blois 2001
Forman W., Churazov E., Jones C., Heinz S., Kraft R., Vikhlinin A., 2017, ApJ, 844, 122
Gaibler V., Khochfar S., Krause M., Silk J., 2012, MNRAS, 425, 438
Gaspari M., Sądowski A., 2017, ApJ, 837, 149
Gaspari M., Brighenti F., Temi P., 2012, MNRAS, 424, 190
Gaspari M., Ruszkowski M., Oh S. P., 2013, MNRAS, 432, 3401
Gaspari M., Churazov E., Nagai D., Lau E. T., Zhuravleva I., 2014, A&A, 569, A67
Gaspari M., Brighenti F., Temi P., 2015, A&A, 579, A62
Gaspari M., Tombesi F., Cappi M., 2020, Nat. Astron., 4, 10
Gastaldello F. et al., 2013, ApJ, 770, 56
Ge J. P., Owen F. N., 1993, AJ, 105, 778
Gendron-Marsolais M. et al., 2017, ApJ, 848, 26
Ghizzardi S., Rossetti M., Molendi S., 2010, A&A, 516, A32+
Giacintucci S., Venturi T., Murgia M., Dallacasa D., Athreya R., Bardelli S., Mazzotta P., Saikia D. J., 2007, A&A, 476, 99
Giacintucci S. et al., 2011, ApJ, 732, 95
Giacintucci S., Markevitch M., Venturi T., Clarke T. E., Cassano R., Mazzotta P., 2014, ApJ, 781, 9
Giacintucci S., Markevitch M., Cassano R., Venturi T., Clarke T. E., Brunetti G., 2017, ApJ, 841, 71
Giovannini G., Cotton W. D., Feretti L., Lara L., Venturi T., 1998, ApJ, 493, 632
Gitti M., McNamara B. R., Nulsen P. E. J., Wise M. W., 2007, ApJ, 660, 1118
Godfrey L. E. H., Shabala S. S., 2016, MNRAS, 456, 1172
Grossová R. et al., 2019, MNRAS, 488, 1917
Guo F., Oh S. P., 2008, MNRAS, 384, 251
Hamer S. L. et al., 2016, MNRAS, 460, 1758
Hardcastle M. J., Evans D. A., Croston J. H., 2006, MNRAS, 370, 1893
Hardcastle M. J., Evans D. A., Croston J. H., 2007, MNRAS, 376, 1849
Hardcastle M. J. et al., 2019, A&A, 622, A12
Hart Q. N., Stocke J. T., Hallman E. J., 2009, ApJ, 705, 854
Heckman T. M., Best P. N., 2014, ARA&A, 52, 589
Hillel S., Soker N., 2017, ApJ, 845, 91
Hine R. G., Longair M. S., 1979, MNRAS, 188, 111
Hines D. C., Wills B. J., 1993, ApJ, 415, 82
Hlavacek-Larrondo J., Fabian A. C., Sanders J. S., Taylor G. B., 2011, MNRAS, 415, 3520
Hlavacek-Larrondo J., Fabian A. C., Edge A. C., Ebeling H., Sanders J. S., Hogan M. T., Taylor G. B., 2012, MNRAS, 421, 1360
Hlavacek-Larrondo J. et al., 2013a, ApJ, 777, 163
Hlavacek-Larrondo J., Fabian A. C., Edge A. C., Ebeling H., Allen S. W., Sanders J. S., Taylor G. B., 2013b, MNRAS, 431, 1638
Hlavacek-Larrondo J. et al., 2015, ApJ, 805, 35
Hogan M. T. et al., 2015, MNRAS, 453, 1201
Ineson J., Croston J. H., Hardcastle M. J., Mingo B., 2017, MNRAS, 467, 1586
Jacob S., Pfrommer C., 2017, MNRAS, 467, 1478
Jetha N. N., Ponman T. J., Hardcastle M. J., Croston J. H., 2007, MNRAS, 376, 193
Jetha N. N., Hardcastle M. J., Babul A., O'Sullivan E., Ponman T. J., Raychaudhury S., Vrtilek J., 2008, MNRAS, 384, 1344
Jiang Y.-F., Oh S. P., 2018, ApJ, 854, 5
Johnstone R. M., Allen S. W., Fabian A. C., Sanders J. S., 2002, MNRAS, 336, 299
Kale R., Venturi T., Giacintucci S., Dallacasa D., Cassano R., Brunetti G., Macario G., Athreya R., 2013, A&A, 557, A99
Kale R. et al., 2015, A&A, 579, A92
Kim W.-T., Narayan R., 2003, ApJ, 596, L139
Kirkpatrick C. C., McNamara B. R., 2015, MNRAS, 452, 4361
Kokotanekov G. et al., 2017, A&A, 605, A48
Kokotanekov G., Wise M. W., de Vries M., Intema H. T., 2018, A&A, 618, A152
Kolokythas K., O'Sullivan E., Raychaudhury S., Giacintucci S., Gitti M., Babul A., 2018, MNRAS, 481, 1550
Laing R. A., Bridle A. H., 2014, MNRAS, 437, 3405
Laing R. A., Guidetti D., Bridle A. H., Parma P., Bondi M., 2011, MNRAS, 417, 2789
Lakhchaura K. et al., 2018, MNRAS, 481, 4472
Li Y., Bryan G. L., 2014a, ApJ, 789, 54
Li Y., Bryan G. L., 2014b, ApJ, 789, 153
Luo Q., Sadler E. M., 2010, ApJ, 713, 398
Machacek M. E., Jerius D., Kraft R., Forman W. R., Jones C., Randall S., Giacintucci S., Sun M., 2011, ApJ, 743, 15
Magliocchetti M., Brüggen M., 2007, MNRAS, 379, 260
Ma C.-J., McNamara B. R., Nulsen P. E. J., 2013, ApJ, 763, 63
Markevitch M., Vikhlinin A., 2007, Phys. Rep., 443, 1
Markevitch M. et al., 2000, ApJ, 541, 542
Marriage T. A. et al., 2011, ApJ, 737, 61
Martizzi D., Quataert E., Faucher-Giguère C.-A., Fielding D., 2019, MNRAS, 483, 2465
Mazzotta P., Kaastra J. S., Paerels F. B., Ferrigno C., Colafrancesco S., Mewe R., Forman W. R., 2002, ApJ, 567, L37
Mazzotta P., Edge A. C., Markevitch M., 2003, ApJ, 596, 190
McDonald M., Veilleux S., 2009, ApJ, 703, L172
McDonald M., Veilleux S., Rupke D. S. N., Mushotzky R., 2010, ApJ, 721, 1262
McDonald M., Roediger J., Veilleux S., Ehlert S., 2014, ApJ, 791, L30
McDonald M. et al., 2016, ApJ, 817, 86
McDonald M., Gaspari M., McNamara B. R., Tremblay G. R., 2018, ApJ, 858, 45
McKean J. P. et al., 2016, MNRAS, 463, 3143
McNamara B. R., Nulsen P. E. J., 2007, ARA&A, 45, 117
McNamara B. R., Nulsen P. E. J., 2012, New J. Phys., 14, 055023
McNamara B. R., Wise M. W., Murray S. S., 2004, ApJ, 601, 173
McNamara B. R., Nulsen P. E. J., Wise M. W., Rafferty D. A., Carilli C., Sarazin C. L., Blanton E. L., 2005, Nature, 433, 45
McNamara B. R., Kazemzadeh F., Rafferty D. A., Bîrzan L., Nulsen P. E. J., Kirkpatrick C. C., Wise M. W., 2009, ApJ, 698, 594
McNamara B. R., Russell H. R., Nulsen P. E. J., Hogan M. T., Fabian0 A. C., Pulido F., Edge A. C., 2016, ApJ, 830, 79
Meece G. R., Voit G. M., O'Shea B. W., 2017, ApJ, 841, 133
Merloni A., Heinz S., 2007, MNRAS, 381, 589
Mittal R., Whelan J. T., Combes F., 2015, MNRAS, 450, 2564
Morabito L. K., 2016, PhD thesis, Leiden University
Morganti R., Fanti R., Gioia I. M., Harris D. E., Parma P., de Ruiter H., 1988, A&A, 189, 11
Nulsen P. E. J., Hambrick D. C., McNamara B. R., Rafferty D., Birzan L., Wise M. W., David L. P., 2005, ApJ, 625, L9
Nulsen P., Jones C., Forman W., Churazov E., McNamara B., David L., Murray S., 2009, in Heinz S., Wilcots E., eds, AIP Conf. Ser. Vol. 1201, Radio Mode Outbursts in Giant Elliptical Galaxies. Astron Soc. Pac., San Francisco, p. 198
Nulsen P. E. J. et al., 2013, ApJ, 775, 117
O'Dea K. P. et al., 2010, ApJ, 719, 1619
O'Sullivan E., Giacintucci S., David L. P., Gitti M., Vrtilek J. M., Raychaudhury S., Ponman T. J., 2011, ApJ, 735, 11
O'Sullivan E. et al., 2012, MNRAS, 424, 2971
O'Sullivan E. et al., 2017, MNRAS, 472, 1482

O'Sullivan E., Schellenberger G., Burke D. J., Sun M., Vrtilek J. M., David L. P., Sarazin C., 2019, MNRAS, 488, 2925
Ogiya G., Biernacki P., Hahn O., Teyssier R., 2018, preprint (arXiv:e-print)
Owen F. N., Eilek J. A., 1998, ApJ, 493, 73
Owen F. N., Ledlow M. J., 1997, ApJS, 108, 41
Pandge M. B., Vagshette N. D., David L. P., Patil M. K., 2012, MNRAS, 421, 808
Pandge M. B., Sonkamble S. S., Parekh V., Dabhade P., Parmar A., Patil M. K., Raychaudhury S., 2019, ApJ, 870, 62
Parma P., de Ruiter H. R., Fanti C., Fanti R., 1986, A&AS, 64, 135
Patnaik A. R., Singh K. P., 1988, MNRAS, 234, 847
Perucho M., Martí J. M., Laing R. A., Hardee P. E., 2014, MNRAS, 441, 1488
Peterson J. R., Fabian A. C., 2006, Phys. Rep., 427, 1
Pfrommer C., 2013, ApJ, 779, 10
Pinto C., Bambic C. J., Sanders J. S., Fabian A. C., McDonald M., Russell H. R., Liu H., Reynolds C. S., 2018, MNRAS, 480, 4113
Planck Collaboration XXIX, 2014, A&A, 571, 29
Pope E. C. D., Babul A., Pavlovski G., Bower R. G., Dotter A., 2010, MNRAS, 406, 2023
Pracy M. B. et al., 2016, MNRAS, 460, 2
Prasad D., Sharma P., Babul A., 2015, ApJ, 811, 108
Prasad D., Sharma P., Babul A., 2017, MNRAS, 471, 1531
Prokhorov D. A., Churazov E. M., 2017, MNRAS, 470, 3388
Pulido F. A. et al., 2018, ApJ, 853, 177
Rafferty D. A., McNamara B. R., Nulsen P. E. J., Wise M. W., 2006, ApJ, 652, 216
Rafferty D. A., McNamara B. R., Nulsen P. E. J., 2008, ApJ, 687, 899
Rafferty D. A., Bîrzan L., Nulsen P. E. J., McNamara B. R., Brandt W. N., Wise M. W., Röttgering H. J. A., 2013, MNRAS, 428, 58
Randall S. W., Jones C., Markevitch M., Blanton E. L., Nulsen P. E. J., Forman W. R., 2009, ApJ, 700, 1404
Randall S. W. et al., 2015, ApJ, 805, 112
Reichardt C. L. et al., 2013, ApJ, 763, 127
Revaz Y., Combes F., Salomé P., 2008, A&A, 477, L33
Reynolds C. S., Balbus S. A., Schekochihin A. A., 2015, ApJ, 815, 41
Rudnick L., Lemmerman J. A., 2009, ApJ, 697, 1341
Ruffa I. et al., 2019, MNRAS, 489, 3739
Russell H. R., McNamara B. R., Edge A. C., Hogan M. T., Main R. A., Vantyghem A. N., 2013, MNRAS, 432, 530
Ruszkowski M., Yang H. Y. K., Reynolds C. S., 2017, ApJ, 844, 13
Sabater J. et al., 2019, A&A, 622, A17
Salomé P., Combes F., 2003, A&A, 412, 657
Sanders J. S., Fabian A. C., 2007, MNRAS, 381, 1381
Sanders J. S., Fabian A. C., Taylor G. B., 2009, MNRAS, 396, 1449
Sarazin C. L., Baum S. A., O'Dea C. P., 1995, ApJ, 451, 125
Savini F. et al., 2019, A&A, 622, A24
Schellenberger G., Vrtilek J. M., David L., O'Sullivan E., Giacintucci S., Johnston-Hollitt M., Duchesne S. W., Raychaudhury S., 2017, ApJ, 845, 84
Sharma P., Parrish I. J., Quataert E., 2010, ApJ, 720, 652
Shimwell T. W. et al., 2019, A&A, 622, A1
Shin J., Woo J.-H., Mulchaey J. S., 2016, ApJS, 227, 31
Sijacki D., Vogelsberger M., Genel S., Springel V., Torrey P., Snyder G. F., Nelson D., Hernquist L., 2015, MNRAS, 452, 575
Silk J., 2013, ApJ, 772, 112
Simpson C., Westoby P., Arumugam V., Ivison R., Hartley W., Almaini O., 2013, MNRAS, 433, 2647
Smolcic V. et al., 2015, Proc. Sci., Exploring AGN Activity over Cosmic Time with the SKA. SISSA, Trieste, PoS #69
Smolčić V. et al., 2009, ApJ, 696, 24
Smolčić V. et al., 2017, A&A, 602, A6
Sonkamble S. S., Vagshette N. D., Pawar P. K., Patil M. K., 2015, Ap&SS, 359, 21
Su Y. et al., 2017, ApJ, 851, 69
Sun M., 2009, ApJ, 704, 1586
Sun M., Jones C., Murray S. S., Allen S. W., Fabian A. C., Edge A. C., 2003, ApJ, 587, 619
Tang X., Churazov E., 2017, MNRAS, 468, 3516
Temi P., Amblard A., Gitti M., Brighenti F., Gaspari M., Mathews W. G., David L., 2018, ApJ, 858, 17
Thomas T., Pfrommer C., 2019, MNRAS, 485, 2977
Tremblay G. R. et al., 2015, MNRAS, 451, 3768
Vagshette N. D., Sonkamble S. S., Naik S., Patil M. K., 2016, MNRAS, 461, 1885
Valentini M., Brighenti F., 2015, MNRAS, 448, 1979
Valentini M. et al., 2020, MNRAS, 491, 2771
van Haarlem M. P. et al., 2013, A&A, 556, A2
van Weeren R. J. et al., 2016, ApJS, 223, 2
Vantyghem A. N., McNamara B. R., Russell H. R., Main R. A., Nulsen P. E. J., Wise M. W., Hoekstra H., Gitti M., 2014, MNRAS, 442, 3192
Vantyghem A. N. et al., 2016, ApJ, 832, 148
Vantyghem A. N. et al., 2019, ApJ, 870, 57
Varenius E. et al., 2015, A&A, 574, A114
Varenius E. et al., 2016, A&A, 593, A86
Voit G. M., Cavagnolo K. W., Donahue M., Rafferty D. A., McNamara B. R., Nulsen P. E. J., 2008, ApJ, 681, L5
Voit G. M., Donahue M., Bryan G. L., McDonald M., 2015, Nature, 519, 203
Voit G. M., Meece G., Li Y., O'Shea B. W., Bryan G. L., Donahue M., 2017, ApJ, 845, 80
Wagner A. Y., Bicknell G. V., Umemura M., 2012, ApJ, 757, 136
Wagner A. Y., Bicknell G. V., Umemura M., Sutherland R. S., Silk J., 2016, Astron. Nachr., 337, 167
Walker S. A., Fabian A. C., Kosec P., 2014, MNRAS, 445, 3444
Walker S. A., Sanders J. S., Fabian A. C., 2018, MNRAS, 481, 1718
Wang Y., Lui F., Shen Z., Wang J., Hu D., Xu H.-G., 2019, ApJ, 870, 132
Weinberger R., Ehlert K., Pfrommer C., Pakmor R., Springel V., 2017, MNRAS, 470, 4530
Werner N. et al., 2014, MNRAS, 439, 2291
White D. A., Jones C., Forman W., 1997, MNRAS, 292, 419
Wiener J., Oh S. P., Guo F., 2013, MNRAS, 434, 2209
Willott C. J., Rawlings S., Blundell K. M., Lacy M., 1999, MNRAS, 309, 1017
Wylezalek D., Zakamska N. L., 2016, MNRAS, 461, 3724
Xu W., Readhead A. C. S., Pearson T. J., Polatidis A. G., Wilkinson P. N., 1995, ApJS, 99, 297
Yang H.-Y. K., Reynolds C. S., 2016, ApJ, 829, 90
Yang H.-Y. K., Gaspari M., Marlow C., 2019, ApJ, 871, 6
Young L. M. et al., 2011, MNRAS, 414, 940
Zhang C., Churazov E., Schekochihin A. A., 2018, MNRAS, 478, 4785
Zhao J.-H., Sumi D. M., Burns J. O., Duric N., 1993, ApJ, 416, 51
Zhuravleva I. et al., 2014, Nature, 515, 85
Zhuravleva I., Allen S. W., Mantz A., Werner N., 2018, ApJ, 865, 53
Zuhone J. A., Roediger E., 2016, J. Plasma Phys., 82, 535820301
ZuHone J. A., Markevitch M., Johnson R. E., 2010, ApJ, 717, 908

This paper has been typeset from a TEX/LATEX file prepared by the author.